Chapter 3
Moving Front Instabilities: From Viscous Fingers to Solution Pipes

Piotr Szymczak

Abstract This set of lectures is devoted to the moving boundary processes in which a more mobile phase advances into a less mobile one. In such cases, the boundary between the phases becomes unstable and breaks into fingers. We are discussing two examples of such processes: viscous fingering, which is a classical example of unstable growth, and reactive-infiltration instability, which occurs in the process of dissolving fractures and porous rocks.

3.1 Moving Front Instabilities

> The moving finger writes; and, having writ,
> moves on: nor all thy piety nor wit
> shall lure it back to cancel half a line,
> nor all thy tears wash out a word of it.
>
> —Omar Khayyám *Rubáiyát*

Many physical processes involving moving boundaries produce fingering patterns. Well-known examples include viscous fingering (Hill, 1952; Saffman & Taylor, 1958; Wooding, 1969; Paterson, 1981; Homsy, 1987), electrochemical deposition (Kuhn & Argoul, 1994; Meakin, 1998), growth of bacterial colonies (Golding et al., 1998; Ben-Jacob et al., 1992), crystallization in supercooled liquids (Couder et al., 1990, 2005), or dissolution of porous medium (Daccord, 1987; Hoefner & Fogler, 1988). Some of the ramified, intricate patterns which emerge in these processes are shown in Fig. 3.1. In all of these processes, the advancing interface becomes unstable if the mobility of the invading phase is larger than that of a displaced phase. Small perturbations of the interface grow and transform into fingers, which compete for the fluxes which feed them. A paradigm of these processes is a (two-phase) Laplacian growth problem

---

P. Szymczak (✉)
Institute of Theoretical Physics, Faculty of Physics, University of Warsaw, Warsaw, Poland
e-mail: piotrek@fuw.edu.pl

M. Berhanu and P. Szymczak (eds.), *Fluid Flow and Phase Change of a Solid*,
CISM International Centre for Mechanical Sciences 619,
https://doi.org/10.1007/978-3-032-11979-7_3

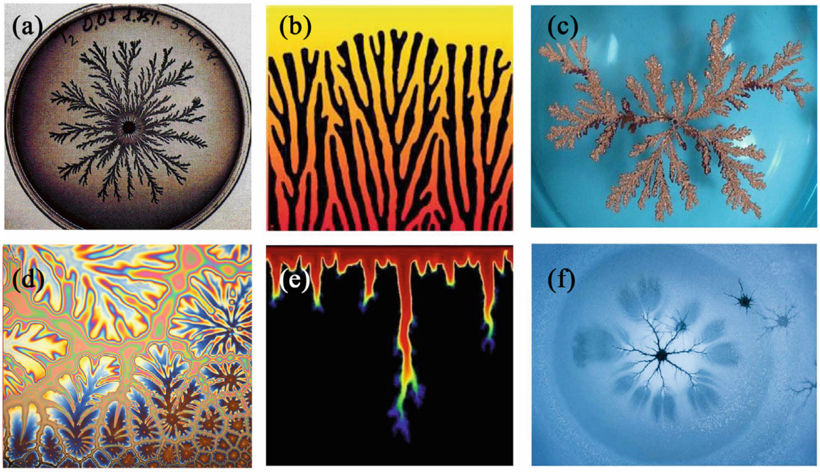

Fig. 3.1 Fingering patterns arising as the result of moving-front instabilities: **a** bacterial growth (Ben-Jacob et al., 1998), **b** combustion of a thin solid (Zik et al., 1998), **c** electrodeposition: copper aggregate formed from a copper sulfate solution in an electrodeposition cell (photo by Kevin R. Johnson, distributed under CC BY 2.5 license) **d** viscous fingering in a TiO_2 sol-gel thin film (photo by Claire Trease, Kingston University, distributed under CC BY-SA 4.0). **e** fracture dissolution (Szymczak & Ladd, 2006), **f** ice star formation (Grodzki & Szymczak, 2019) (photo courtesy of Martin Mecnarowski; www.photomecan.eu)

(Howison, 2000), known also as the Muskat problem (Muskat, 1937), in which the fluxes are associated with the harmonic field. The equations governing the growth are then given by:

$$\nabla^2\Psi_1(\boldsymbol{x},t)=0 \qquad \boldsymbol{x}\in\Omega \tag{3.1}$$

$$\nabla^2\Psi_2(\boldsymbol{x},t)=0 \qquad \boldsymbol{x}\in\bar{\Omega} \tag{3.2}$$

$$\Psi_1(\boldsymbol{x},t)=\Psi_2(\boldsymbol{x},t) \qquad \boldsymbol{x}\in\Gamma_t \tag{3.3}$$

$$(-M_1\nabla\Psi_1(\boldsymbol{x},t))_n=(-M_2\nabla\Psi_2(\boldsymbol{x},t))_n \qquad \boldsymbol{x}\in\Gamma_t \tag{3.4}$$

$$U_n(t)=\alpha\,(-M_2\nabla\Psi_2(\boldsymbol{x},t))_n \qquad \boldsymbol{x}\in\Gamma_t \tag{3.5}$$

In the above, Ω denotes an invading phase, $\bar{\Omega}$—displaced phase and Γ_t is an interface, as depicted in Fig. 3.2. Next, Ψ stands for the field which is driving the growth (e.g. pressure in viscous fingering or temperature in solidification). The associated flux is given by $J_i=-M_i\nabla\Psi_i$, where M_i is the mobility of phase i. Both the field and the normal component of the flux are assumed to be continuous across the interface. Finally, Eq. (3.5) links the advancement velocity of the interface (U_n) and the flux, with α being a proportionality constant and subscript n denoting the component normal to Γ. We will assume the system to be (quasi-)two-dimensional. In fact, all of the systems in Fig. 3.1 are quasi-2D, which is not a coincidence—branch

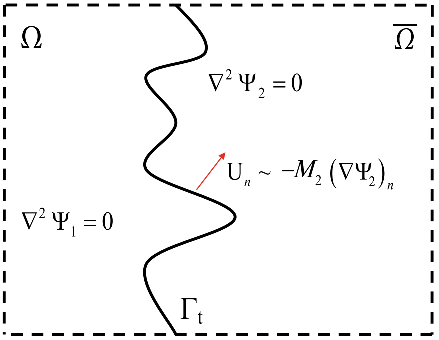

Fig. 3.2 Schematic of the system with an invading phase Ω and a displaced one $\bar{\Omega}$. The interface, Γ moves with velocity U proportional to the field gradient

competition for flux is much stronger in 2D than in 3D, making two dimensions far more favorable for pattern formation.

Equations (3.1)–(3.5) should be supplemented with appropriate far-field boundary conditions, which depend on a particular geometry in which growth takes place. For rectangular geometry one usually imposes the condition of a uniform flux at infinity

$$\lim_{x\to-\infty} (-M_1 \nabla \Psi_1(\boldsymbol{x}, t)) = \hat{\boldsymbol{e}}_x = \lim_{x\to\infty} (-M_2 \nabla \Psi_2(\boldsymbol{x}, t)) \tag{3.6}$$

where x is the direction of front propagation.

An important dimensionless parameter characterizing the system is the mobility ratio, $\Gamma = M_2/M_1$. Whenever $M_1 > M_2$, the flux of the field over the crest of a small protrusion of the interface is larger than that in the surrounding flat regions and thus initially flat interface becomes unstable and breaks into fingers. The aspect ratio of the fingers tends to increase in time, since the field gradient is always the largest at their tips. Finally, the fingers become stabilized by surface tension, kinetic undercooling or other short-scale regularization mechanisms, which depend on a particular problem at hand. Note that in the limit $\Gamma \to 0$ the problem reduces to a classical, one phase Laplacian growth (Gustafsson et al., 2014), driven by one field only (Ψ_2) with the condition $\Psi_2 = 0$ imposed on the moving boundary.

In the following sections, we will explore two examples of such systems. The first example is the well-known Saffman–Taylor (viscous fingering) problem, where one fluid displaces another in a Hele–Shaw cell (i.e., a thin gap between two glass plates), and the field driving the growth is the fluid pressure. The second example involves the dissolution process in a Hele–Shaw cell, but with a soluble bottom. Here, the growth is driven by the interplay of two coupled fields: fluid pressure and the concentration field of a reactant, resulting in more complex dynamics. Before delving into these examples, let us first review the Hele–Shaw flow equations, as both problems involve the Hele–Shaw cell.

3.2 Hele–Shaw Flow

There once was a fellow, Hele–Shaw,
Whose fluid mechanics had no flaw.
He studied with grace,
Fluid flow in tight space,
And his name became science's law.

ChatGPT4o

Where the flow occurs within a Hele–Shaw cell, the fluid flow equations can be significantly simplified. The following derivation is largely based on Acheson (1990). We start from the Navier–Stokes equations describing the fluid motion:

$$\frac{\partial \boldsymbol{v}}{\partial t} + (\boldsymbol{v} \cdot \nabla)\boldsymbol{v} = -\frac{1}{\rho}\nabla p + \nu \Delta \boldsymbol{v} + \boldsymbol{f}, \tag{3.7}$$

where ρ denotes the fluid density, $\boldsymbol{v}$ is the flow field, p represents pressure, ν is the kinematic viscosity, and $\boldsymbol{f}$ is the volume force density (in our case, $\boldsymbol{f} = 0$).

We assume stick boundary conditions along the top and bottom plate of the Hele–Shaw cell

$$\boldsymbol{v}(z = 0) = 0, \;\; \boldsymbol{v}(z = h) = 0, \tag{3.8}$$

where h is the distance between the plates.

Next, let U be the characteristic velocity of the fluid in the xy plane, i.e., $v_x \sim U$ and $v_y \sim U$. The changes in v_x and v_y along z are then of the order of U, thus

$$\frac{\partial v_x}{\partial z} \sim \frac{U}{h}, \quad \frac{\partial v_y}{\partial z} \sim \frac{U}{h}. \tag{3.9}$$

Meanwhile, the changes in v_x in the XY plane are of the order of

$$\frac{\partial v_x}{\partial x} \sim \frac{U}{L}, \quad \frac{\partial v_x}{\partial y} \sim \frac{U}{L}, \tag{3.10}$$

and similarly for v_y. Here, L is the longitudinal size of the cell. A similar estimate can be made for the second derivatives:

$$\frac{\partial^2 v_x}{\partial z^2} \sim \frac{U}{h^2}, \quad \frac{\partial^2 v_x}{\partial x^2} \sim \frac{U}{L^2}, \quad \frac{\partial^2 v_x}{\partial y^2} \sim \frac{U}{L^2}, \tag{3.11}$$

and analogously for v_y. As we see, the derivatives along the z direction are much larger than the respective derivatives along x and y, since $L \gg h$. Hence, the viscous term in the flow equation (3.7) can be approximated as:

$$\nu \Delta \boldsymbol{v} \approx \nu \frac{\partial^2 \boldsymbol{v}}{\partial z^2}. \tag{3.12}$$

Furthermore, from the incompressibility of the fluid

$$\frac{\partial v_x}{\partial x} + \frac{\partial v_y}{\partial y} + \frac{\partial v_z}{\partial z} = 0, \tag{3.13}$$

we infer that v_z needs to be of an order of Uh/L, so, up to the leading order

$$\boldsymbol{v} \sim U\left(1, 1, \frac{h}{L}\right). \tag{3.14}$$

Finally then the viscous term in the Navier–Stokes equation can be approximated by

$$\nu \frac{\partial^2 \boldsymbol{v}}{\partial z^2} \approx \frac{\nu U}{h^2}\left(1, 1, \frac{h}{L}\right). \tag{3.15}$$

The nonlinear term can similarly be approximated by

$$(\boldsymbol{v} \cdot \nabla)\boldsymbol{v} \approx \frac{U^2}{L}\left(1, 1, \frac{h}{L}\right). \tag{3.16}$$

The characteristic time scale T associated with our system is given by:

$$T \sim \frac{L}{U}, \tag{3.17}$$

thus the time-dependent term in equation (3.7) is again of the order:

$$\frac{\partial \boldsymbol{v}}{\partial t} \approx \frac{U^2}{L}\left(1, 1, \frac{h}{L}\right). \tag{3.18}$$

Analysis of the relations (3.15)–(3.18) allows us to conclude that the ratio of the nonlinear term ($(\boldsymbol{v} \cdot \nabla)\boldsymbol{v}$) to the viscous term in equation (3.7) is of the order:

$$\frac{UL\rho}{\eta}\frac{h^2}{L^2} = \mathrm{Re}\frac{h^2}{L^2} \ll 1, \tag{3.19}$$

where Re is the Reynolds number. Note that we do not need to assume $\mathrm{Re} \ll 1$, since the separation of lengthscales between the vertical and horizontal direction, $\frac{h}{L} \ll 1$ allows us to neglect the nonlinear term in the flow equations even for relatively high

Reynolds numbers. Similar reasoning allows us to neglect the time-dependent term, and ultimately (3.7) reduces to:

$$\nabla p = \eta \frac{\partial^2 \boldsymbol{v}}{\partial z^2}. \tag{3.20}$$

Additionally, since v_z is smaller than v_x and v_y by a factor of h/L, we infer that $\frac{\partial p}{\partial z} \ll \frac{\partial p}{\partial x}, \frac{\partial p}{\partial y}$. Thus p is, to a first approximation, a function of x and y alone, $p \sim p(x, y)$. This means that a two-dimensional velocity field $\boldsymbol{v}' = (v_x, v_y)$ is sufficient for describing the system. Integrating equation (3.20) under this assumption leads us to:

$$\boldsymbol{v}' = \frac{\nabla p}{2\eta} z^2 + \boldsymbol{A} z + \boldsymbol{B} \tag{3.21}$$

where the gradient operator ∇ acts in (x, y) space only.

Taking into account the stick boundary conditions at $z = 0$ and $z = h$ we can find the $\boldsymbol{A}$ and $\boldsymbol{B}$ vectors, getting finally

$$\boldsymbol{v}' = \frac{\nabla p}{2\eta}(z^2 - hz). \tag{3.22}$$

For further considerations, it will be more convenient to use the total, z-integrated fluid flux:

$$\boldsymbol{q}(x, y) = \int_0^h \boldsymbol{v}'(z) \mathrm{d}z = \frac{\nabla p}{2\eta} \int_0^h (z^2 - hz) \mathrm{d}z = -\frac{h^3 \nabla p}{12\eta}, \tag{3.23}$$

which can be written as:

$$\boldsymbol{q} = -M \nabla p, \tag{3.24}$$

where $M = h^3/12\eta$ is the mobility of the system.

Equation (3.24) is known as the Poiseuille law. A similar relationship between velocity and pressure gradient is observed in the flow of fluids through porous materials and known as the Darcy law (see Bear, 1972). The Poiseuille law needs to be supplemented with the incompressibility condition (3.13). Integrating Eq. (3.13) over z and taking into account stick boundary conditions at the top and bottom plate of the Hele–Shaw cell, we get

$$\nabla \cdot \boldsymbol{q}(x, y) = 0, \tag{3.25}$$

which, when combined with (3.24) leads to the pressure equation

$$\boldsymbol{\nabla} \cdot (M \boldsymbol{\nabla} p) = 0. \tag{3.26}$$

If the distance between the upper and lower surface is constant, $h(x, y) = const.$, and the fluid has a constant viscosity, then M is constant as well and (3.26) transforms into the Laplace equation

$$\nabla^2 p = 0, \tag{3.27}$$

exactly as in Eqs. (3.1)–(3.2).

3.3 Viscous Fingering

> Pour a liquid, especially oil, between two fine
> polished plates of marble, compressed close
> together; upon parting them again, the oil
> will be found to have run, into beautiful
> and delicate ramified tracts
>
> —Emanuel Mendes da Costa *A Natural History of Fossils*

Equipped with the thin-film flow equations, we can now consider a classical viscous fingering (Saffman–Taylor) problem (Fig. 3.3). Let us imagine a rectangular Hele–Shaw cell initially filled with a fluid of viscosity η_2. Fluid of viscosity η_1 is then injected from the $x = -\infty$ side with a constant mean injection velocity V, i.e.:

$$\lim_{x\to-\infty} \boldsymbol{q}_1 = Vh\hat{\boldsymbol{e}}_x. \tag{3.28}$$

To proceed, we introduce a parameterization of the phase boundary:

$$\boldsymbol{r}_f = x_f(y)\hat{\boldsymbol{e}}_x + y\hat{\boldsymbol{e}}_y, \tag{3.29}$$

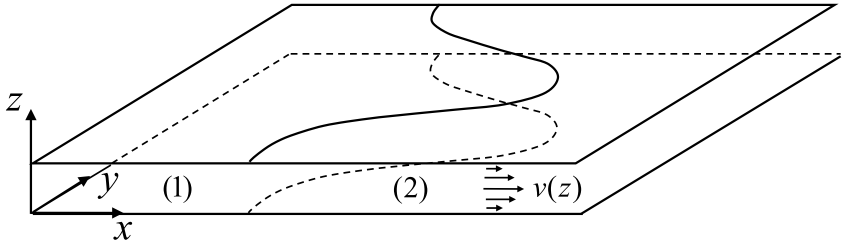

Fig. 3.3 Sketch of a Hele–Shaw cell with two fluids

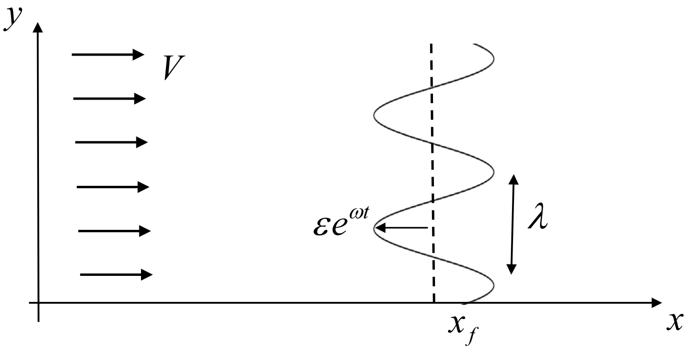

Fig. 3.4 Parametrization of the front

as illustrated in Fig. 3.4. Note that the phase boundary moves with velocity of each of the fluids on that boundary, i.e.

$$h\boldsymbol{n}\cdot\frac{\mathrm{d}\boldsymbol{r}_f(s)}{\mathrm{d}t}=\boldsymbol{q}_1\cdot\boldsymbol{n}\bigg|_{\boldsymbol{r}_f}=\boldsymbol{q}_2\cdot\boldsymbol{n}\bigg|_{\boldsymbol{r}_f}, \tag{3.30}$$

where $\boldsymbol{n}$ is the vector normal to the interface. The equations governing the evolution of the system are then:

- Laplace's equation for pressure (3.27), in each phase (since both phases have constant viscosities)

$$\nabla^2 p_i = 0;$$

- Darcy's law for the flow in the Hele–Shaw cell (3.24)

$$\boldsymbol{q}_i=-M_i\nabla p_i, \qquad M_i=\frac{h^3}{12\eta_i},$$

along with the boundary condition (3.28), and continuity relations for pressure and fluid flux along the boundary of the phases:

$$(p_1-p_2)\bigg|_{\boldsymbol{r}_f}=\gamma(\kappa_1+\kappa_2), \tag{3.31}$$

$$\boldsymbol{q}_1\cdot\boldsymbol{n}\bigg|_{\boldsymbol{r}_f}=\boldsymbol{q}_2\cdot\boldsymbol{n}\bigg|_{\boldsymbol{r}_f}. \tag{3.32}$$

The finite pressure drop in (3.31) is connected with the surface tension effects: γ is the surface tension coefficient, and κ_1, κ_2 represent the curvatures of the surface along two perpendicular planes. The flow field calculated from the above equations can then be used to track the evolution of the phase boundary (3.30). The solution of the equations will be divided into two stages. First, we will consider the case of a flat, homogeneous front, and then perform a linear stability analysis.

3.4 Time-Invariant Solutions

> Time and Space died yesterday.
> We already live in the absolute,
> because we have created eternal, omnipresent speed.
>
> —F.T. Marinetti, *The Founding and Manifesto of Futurism*

Let us first consider the situation where the front is flat, thus all of the fields depend on x coordinate only. This means, in particular, that $\partial p_i^0/\partial y = 0$ and $\partial x_f^0/\partial y = 0$, where the superscript '0' denotes solutions that are uniform in y. The Laplace equation then reduces to:

$$\frac{\partial^2 p_i^0}{\partial x^2} = 0. \tag{3.33}$$

The solutions of this equation, taking into account the boundary conditions, are given by:

$$p_1^0 = -\frac{q_0}{M_1}(x - Vt), \qquad x < Vt \tag{3.34}$$

$$p_2^0 = -\frac{q_0}{M_2}(x - Vt) - \gamma\kappa_1, \qquad x > Vt, \tag{3.35}$$

where we take $p_1^0(x = Vt) = 0$ as the reference point for the pressure field and $q_0 = hV$. The curvature $\kappa_1 = 2/h$ is constant and corresponds to the meniscus along the z axis. The flow field is then uniform

$$\boldsymbol{q}_1^0 = \boldsymbol{q}_2^0 = q_0\hat{\boldsymbol{e}}_x. \tag{3.36}$$

Taking into account such a flow field, the front propagation equation (3.30) becomes simply

$$\frac{\partial x_f^0}{\partial t} = V, \tag{3.37}$$

so that

$$x_f^0(t) = Vt. \tag{3.38}$$

It is convenient to re-write the above results in the moving frame coordinates, $\bar{x} = x - Vt$ and $\bar{t} = t$. The pressure then becomes time-independent

$$p_1^0(\bar{x}, \bar{t}) = -\frac{q_0}{M_1}\bar{x}, \tag{3.39}$$

$$p_2^0(\bar{x},\bar{t}) = -\frac{q_0}{M_2}\bar{x} - \gamma\kappa_1, \tag{3.40}$$

whereas the front stays at $\bar{x} = 0$

$$\bar{x}_f^0(\bar{t}) = 0. \tag{3.41}$$

3.5 Stability Analysis

> But for its absolute self; a life of peace,
> Stability without regret or fear;
> That hath been, is, and shall be evermore!
>
> —William Wordsworth *The Excursion*

Linear stability analysis involves introducing infinitesimally small disturbances to the base solutions (3.39)–(3.41). For example:

$$\bar{x}_f \longrightarrow \bar{x}_f^0 + \delta\bar{x}_f, \tag{3.42}$$

$$p_i \longrightarrow p_i^0 + \delta p_i, \tag{3.43}$$

$$\boldsymbol{q}_i \longrightarrow \boldsymbol{q}_i^0 + \delta\boldsymbol{q}_i. \tag{3.44}$$

Such forms of solutions are then substituted into equations (3.24) and (3.27), neglecting the quadratic and higher-order terms in the disturbances during the solution process. It should also be noted that the disturbance of the front affects its curvature, so the non-zero factor κ_2 from condition (3.31) needs to be taken into account. In implementing this approach, one typically works in the moving front frame, as then the base solutions are stationary, with the time dependence arising solely from the growth of disturbances themselves.

The shape of the disturbance can be arbitrary; however, due to the linearity of the equations, each Fourier component can be considered separately, e.g.:

$$\delta\bar{x}_f = \varepsilon(t)\sin(ky). \tag{3.45}$$

By substituting the disturbances into equation (3.27), we obtain:

$$\Delta\delta p_i = 0. \tag{3.46}$$

The solutions to this equations are given by:

$$\begin{aligned} \delta p_1 &= \delta A_1 \sin(ky)\exp(k\bar{x}), \\ \delta p_2 &= \delta A_2 \sin(ky)\exp(-k\bar{x}), \end{aligned} \tag{3.47}$$

with $k > 0$, as required to satisfy the boundary conditions:

$$\lim_{\bar{x}\to-\infty} \delta\boldsymbol{q}_1 = 0, \quad \lim_{\bar{x}\to\infty} \delta\boldsymbol{q}_2 = 0. \tag{3.48}$$

Next, the Darcy's law takes the form:

$$\delta\boldsymbol{q}_i = -M_i \nabla \delta p_i. \tag{3.49}$$

The next step requires some care, as we need to introduce the disturbance into the continuity conditions (3.31) and (3.32). These relations hold not at $\bar{x}_f^0 = 0$ but at the actual (i.e. perturbed) position of the front, i.e. at $\bar{x}_f^0 + \delta\bar{x}_f$. Thus, we need to carefully expand all the involved functions in a Taylor series up to the linear term in the perturbation. For example,

$$(p^0 + \delta p)(\bar{x}_f^0 + \delta\bar{x}_f) \approx p^0(\bar{x}_f^0) + \delta p(\bar{x}_f^0) + \left.\frac{\partial p^0}{\partial \bar{x}}\right|_{\bar{x}_f^0} \delta\bar{x}_f.$$

Calculating this on both sides of the front leads to

$$\left(p_1^0 - p_2^0\right)_{\bar{x}_f^0} + \left(\delta p_1 - \delta p_2\right)_{\bar{x}_f^0} + \delta\bar{x}_f \left(\frac{\partial p_1^0}{\partial \bar{x}} - \frac{\partial p_2^0}{\partial \bar{x}}\right)_{\bar{x}_f^0} = \gamma(\kappa_1 + \kappa_2). \tag{3.50}$$

Using (3.39)–(3.40) and remembering that in the moving frame $\bar{x}_f^0 = 0$, we get

$$\left(p_1^0 - p_2^0\right)_{\bar{x}=0} = \gamma\kappa_1 \tag{3.51}$$

$$\left(\frac{\partial p_1^0}{\partial \bar{x}} - \frac{\partial p_2^0}{\partial \bar{x}}\right)_{\bar{x}=0} = -\frac{q_0}{M_1} + \frac{q_0}{M_2}. \tag{3.52}$$

On the other hand, using (3.47) we obtain

$$\left(\delta p_1 - \delta p_2\right)_{\bar{x}=0} = \left(\delta A_1 - \delta A_2\right) \sin(ky). \tag{3.53}$$

Putting the above into (3.50) leads to

$$\left(\delta A_1 - \delta A_2\right) \sin(ky) + \varepsilon \sin(ky) \left(-\frac{q_0}{M_1} + \frac{q_0}{M_2}\right) = \gamma\kappa_2 \tag{3.54}$$

where we also used (3.45). The curvature, κ_2 of the curve $\bar{x}_f(y)$, defined as positive for a convex tip, can be expressed as

$$\kappa_2(y) = -\frac{d^2\bar{x}_f}{dy^2} \left(1 + \left(\frac{d\bar{x}_f}{dy}\right)^2\right)^{-3/2}, \tag{3.55}$$

which up to the linear order in ε is simply

$$\kappa_2 = \frac{d^2 \bar{x}_f}{dy^2} = \varepsilon \frac{\partial^2 \sin(ky)}{\partial y^2} = \varepsilon k^2 \sin(ky). \tag{3.56}$$

Finally then

$$\delta A_1 - \delta A_2 + \varepsilon q_0 \left(\frac{1}{M_2} - \frac{1}{M_1} \right) = k^2 \varepsilon \gamma. \tag{3.57}$$

The second continuity condition at the front involves normal components of the fluid flux

$$\boldsymbol{q}_1 \cdot \boldsymbol{n} \Big|_{\delta \bar{x}_f} = \boldsymbol{q}_2 \cdot \boldsymbol{n} \Big|_{\delta \bar{x}_f}. \tag{3.58}$$

To proceed, let us calculate the normal vector to the perturbed front. Starting from

$$\bar{\boldsymbol{r}}_f = \delta \bar{x}_f \hat{\boldsymbol{e}}_x + y \hat{\boldsymbol{e}}_y = \varepsilon \sin(ky) \hat{\boldsymbol{e}}_x + y \hat{\boldsymbol{e}}_y, \tag{3.59}$$

we observe that the tangent vector to the front is proportional to

$$\boldsymbol{t} \sim \frac{d\boldsymbol{r}_f}{dy} \sim \hat{\boldsymbol{e}}_y + \varepsilon k \cos(ky) \hat{\boldsymbol{e}}_x, \tag{3.60}$$

thus the (normalized) normal vector is

$$\boldsymbol{n}(y) = \frac{\hat{\boldsymbol{e}}_x - \varepsilon k \cos(ky) \hat{\boldsymbol{e}}_y}{\sqrt{1 + \varepsilon^2 k^2 \cos^2(ky)}} \approx \hat{\boldsymbol{e}}_x - \varepsilon k \cos(ky) \hat{\boldsymbol{e}}_y. \tag{3.61}$$

The last equality demonstrates that the parameterisation of the front using the arclength and the y-variable yields the same results, up to the linear terms in ε. Importantly, at the lowest order, the normal vector can be approximated by simply $\hat{e}_x$, a fact which will prove to be handy.

Next, to obtain the fluid flux at the front, we calculate the pressure gradient by directly differentiating (3.47)

$$\nabla p_i = -\frac{q_0}{M_i} \hat{\boldsymbol{e}}_x + k \delta A_i \cos(ky) e^{\pm k \bar{x}} \hat{\boldsymbol{e}}_y \pm k \delta A_i \sin(ky) e^{\pm k \bar{x}} \hat{e}_x, \tag{3.62}$$

with the upper sign for $i = 1$ and the lower sign for $i = 2$. We then calculate its normal component at the front, up to the first order in ε. Only the x-component survives, as the y-component appears only at the second order:

$$\nabla p_i \cdot \boldsymbol{n} \approx -\frac{q_0}{M_i} \pm k \delta A_i \sin(ky) e^{\pm k \delta \bar{x}_f} \approx -\frac{q_0}{M_i} \pm k \delta A_i \sin(ky), \tag{3.63}$$

where $e^{\pm k \delta \bar{x}_f}$ was approximated by 1 up to lowest order in the perturbation.

The continuity condition for the normal velocity at the front

$$-M_1\nabla p_1\cdot\boldsymbol{n}=-M_2\nabla p_2\cdot\boldsymbol{n}, \tag{3.64}$$

can then be recast as

$$\delta A_1M_1=-\delta A_2M_2. \tag{3.65}$$

Next, expressing δA_2 in terms of δA_1 and substituting it into (3.57), we get

$$\delta A_1=\frac{\varepsilon k^2\gamma M_2}{M_1+M_2}-\frac{\varepsilon q_0(M_1-M_2)}{M_1(M_1+M_2)}. \tag{3.66}$$

Finally, we have the front propagation equation (3.30), which, after introducing perturbations, yields

$$h\frac{\partial\delta\bar{x}_f}{\partial t}=\delta q_{1n}\bigg|_{x_f^0}. \tag{3.67}$$

The right hand side can be expressed analogously to (3.64), giving

$$h\frac{\partial\varepsilon\sin(ky)}{\partial t}=-M_1k\delta A_1\sin(ky). \tag{3.68}$$

Substituting (3.66) into the above and using the fact that $q_0=Vh$ leads to

$$\frac{\partial\varepsilon}{\partial t}=\varepsilon k\left(V\frac{M_1-M_2}{M_1+M_2}-\frac{k^2\gamma}{h}\frac{M_1M_2}{M_1+M_2}\right). \tag{3.69}$$

The solution to this is an exponential in time

$$\varepsilon\sim e^{\sigma t}, \tag{3.70}$$

with the growth rate

$$\sigma=k\left(V\frac{M_1-M_2}{M_1+M_2}-\frac{k^2\gamma}{h}\frac{M_1M_2}{M_1+M_2}\right). \tag{3.71}$$

Equation (3.71) defines the so-called dispersion relation, linking the growth rate of the perturbation with the wave number. The range of k for which $\sigma(k)>0$ marks the unstable region: perturbations with such wavevectors will be growing. Conversely, for negative $\sigma(k)$, the corresponding perturbations will decay.

For viscous fingering in the Hele–Shaw cell, this is often expressed in terms of viscosities, since $M_i=\frac{h^3}{12\eta_i}$,

$$\sigma(k)=k\left(V\frac{\eta_2-\eta_1}{\eta_1+\eta_2}-k^2\frac{h^2\gamma}{12(\eta_1+\eta_2)}\right). \tag{3.72}$$

This is a classical result, first obtained by Saffman and Taylor (1958). Let us now highlight a number of key features of this dependence. First, for large wavelengths of the perturbations (small k regime) $\sigma(k)$ is linear

$$\sigma(k) = kV\frac{\eta_2 - \eta_1}{\eta_1 + \eta_2} = kV\frac{M_1 - M_2}{M_1 + M_2}. \tag{3.73}$$

Clearly, this is positive whenever the more mobile phase is pushing the less mobile one. Additionally, shorter wavelengths will be growing faster than the longer ones. Without the stabilizing action of surface tension (represented by the second term in (3.72)), this would lead to the so-called **ultraviolet catastrophe**, with the shortest wavelength growing the fastest.

Next, we introduce the capillary number

$$\mathrm{Ca} = \frac{V\eta_2}{\gamma}, \tag{3.74}$$

which measures the ratio of viscous effects to capillary effects in the system, as well as the mobility ratio

$$\Gamma = \frac{M_2}{M_1} = \frac{\eta_1}{\eta_2}. \tag{3.75}$$

Additionally, we rescale the wavevector by the aperture of the Hele–Shaw cell

$$\tilde{k} = kh. \tag{3.76}$$

This allows us to express the dispersion relation in dimensionless form

$$\tilde{\sigma}(\tilde{k}) \equiv \frac{h}{V}\sigma(\tilde{k}) = \frac{\tilde{k}}{(1+\Gamma)}\left((1-\Gamma) - \tilde{k}^2\frac{1}{12\mathrm{Ca}}\right). \tag{3.77}$$

This relation is shown in Fig. 3.5 for $\mathrm{Ca} = 1$ and $\Gamma = 0$ as well as $\Gamma = 0.5$.

We note in passing that the limit $\Gamma = 0$ is well defined, yielding the dispersion relation of the form

$$\tilde{\sigma}(\tilde{k}) = \tilde{k}\left(1 - \tilde{k}^2\frac{1}{12\mathrm{Ca}}\right). \tag{3.78}$$

By calculating the zeros of $\frac{\partial\tilde{\sigma}}{\partial\tilde{k}}$, we find the most unstable wavevector

$$\tilde{k}_c = 2\sqrt{\mathrm{Ca}(1-\Gamma)}. \tag{3.79}$$

The corresponding wavelength, in dimensional variables, is given by

$$\lambda_c = \pi h\sqrt{\frac{\gamma}{V(\eta_2 - \eta_1)}}. \tag{3.80}$$

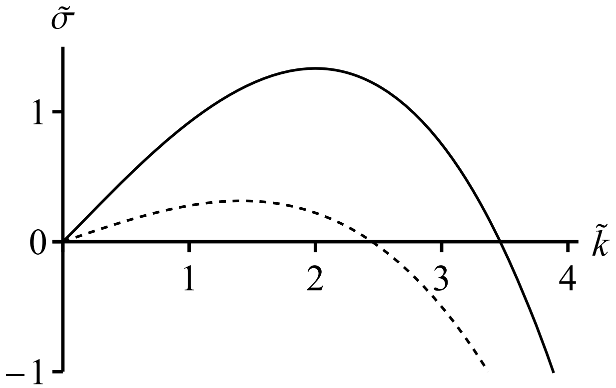

Fig. 3.5 Dispersion relation for the Saffman–Taylor instability (3.77) with $\mathrm{Ca} = 1$, $\Gamma = 0$ (solid line), and $\Gamma = 0.5$ (dashed line)

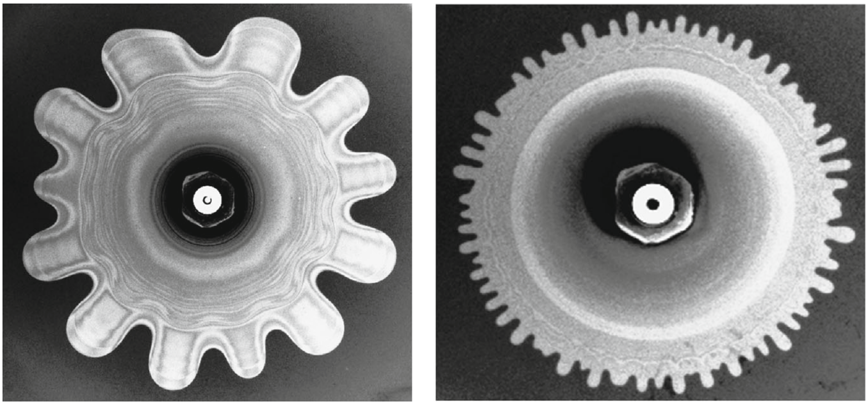

Fig. 3.6 Unstable growth of the air-oil interface in a radial Hele–Shaw cell with a lower (left) and higher (right) injection rate. The figure is courtesy of Harry Swinney (University of Texas at Austin)

As we see, the perturbation wavelength decreases with increasing velocity and increases with the interfacial tension. The former dependence is illustrated in Fig. 3.6.

The zero values of $\tilde{\sigma}(\tilde{k})$ occur at:

$$\tilde{k}_* = 0, \quad \tilde{k}_0 = \sqrt{12\mathrm{Ca}(1-\Gamma)}. \tag{3.81}$$

For $\tilde{k} \in (\tilde{k}_0; \infty)$, $\tilde{\sigma}(\tilde{k})$ is negative, and the front will be stable ($\mathrm{e}^{\tilde{\sigma}t} \to 0$). This stability arises because at large wave numbers ($\tilde{k} > \tilde{k}_0$), or equivalently, small wavelengths ($\lambda = 2\pi h/\tilde{k}$), significant front curvature occurs. High curvature is linked with high surface energy, and thus the surface tension counteracts the propagation of such perturbations. The term associated with surface tension (which includes the inverse

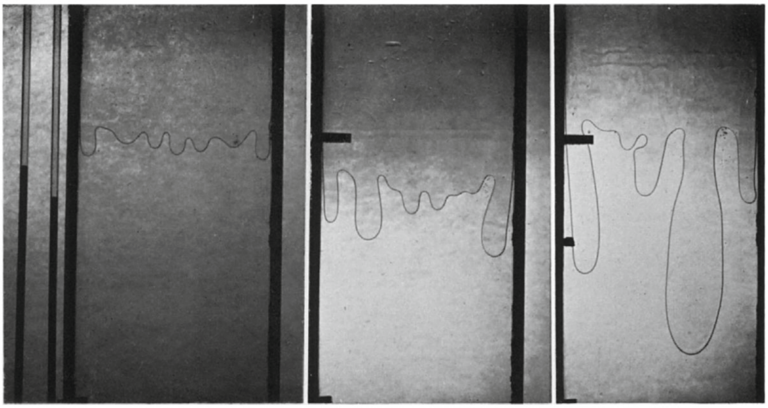

Fig. 3.7 The growth of the air fingers in glycerine (Saffman & Taylor, 1958)

capillary number $1/\mathrm{Ca}$) is proportional to $\tilde{k}^3$ in Eq. (3.72), causing the dispersion relation to diverge towards $-\infty$ for large $\tilde{k}$.

For $\tilde{k} \in (0; \tilde{k}_0)$, $\tilde{\sigma}$ is positive, and the front is unstable ($e^{\tilde{\sigma}t} \rightarrow \infty$). In this region, viscous fingers are formed. The positive sign of $\tilde{\sigma}$ in this range is controlled by the coefficient $\frac{1-\Gamma}{1+\Gamma} = \frac{\eta_2-\eta_1}{\eta_1+\eta_2}$, which multiplies the linear term ($\tilde{k}$) in (3.72). This coefficient is positive when $\eta_2 > \eta_1$, indicating that front instability occurs only when a less viscous fluid (η_1) is injected into a more viscous fluid (η_2). Notably, the condition $\eta_2 > \eta_1$ is also the condition for the existence of zero points (3.81) of the dispersion relation, implying that the front of an infinite extent will always become unstable for large enough wavelengths. In experimental situations, the front is not infinite, leading to a condition on the width of the experimental system W: $W > 2\pi/k_0$. In narrower systems, instabilities are always suppressed.

It is interesting to note what happens to the initial sinusoidal perturbations during the course of evolution. As they grow larger, the linear theory ceases to work, and the fingers begin to interact with each other. Two processes take place here: one is the competition of the fingers for the flow, causing the longer ones to advance ahead of the shorter ones. The other is the merging of the fingers, reducing their total number. As a result, as shown in Fig. 3.7, the pattern coarsens, and eventually, a single finger emerges, which, in the limit of a large capillary number, takes up half of the channel width. Such a final, stable finger-like structure that forms due to the viscous fingering instability is known as the Saffman–Taylor finger (Fig. 3.8a). Interestingly, if the Saffman–Taylor experiment is conducted in a Hele–Shaw cell filled with glass beads (Fig. 3.8b), mimicking a porous medium, the finger appearing in the system has a highly ramified, fractal structure, not unlike diffusion-limited aggregates (Witten & Sander, 1981). This is due to the fact that the local interface curvature controlling the capillary pressure drop depends on the local pore geometry and is thus sensitive to the frozen disorder associated with the structure of this system (Lovoll et al., 2004).

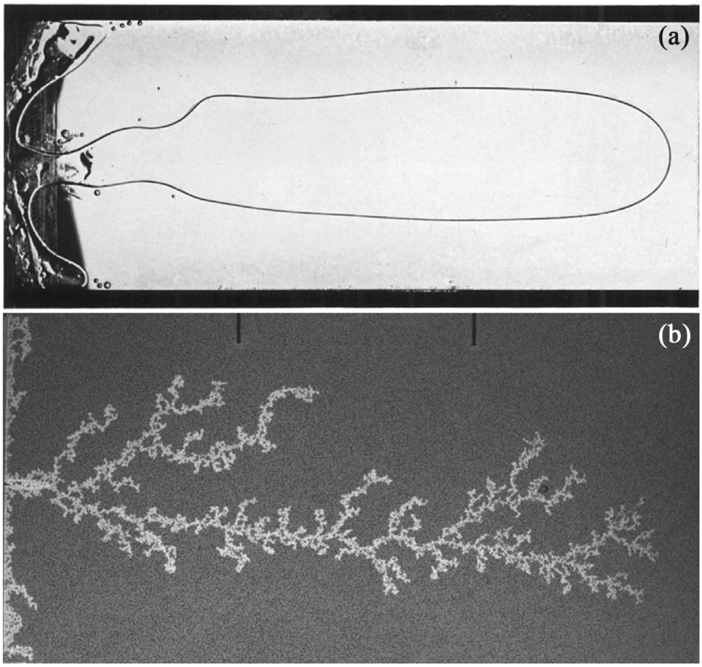

Fig. 3.8 **a**: The Saffman–Taylor finger which appears in the long-time limit in the viscous fingering experiment in a Hele–Shaw cell (Saffman & Taylor, 1958). **b**: The irregular, fractal finger formed in viscous fingering experiment in porous medium, where air was displacing glycerine in a Hele–Shaw cell filled with glass beads (Lovoll et al., 2004). The photo is courtesy of Renaud Toussaint (Institut Terre et Environnement de Strasbourg)

3.6 Reactive-Infiltration Instability

> What is harder than a rock, what softer than water?
> And yet hard rocks are hollowed out by the soft water
>
> —Ovidius *Ars Amatoria*

Let us come back for a moment to the Darcy's law, (3.24), linking the flow rate and the pressure gradient

$$\boldsymbol{q} = -M\nabla p = -\frac{h^3}{12\eta}\nabla p. \tag{3.82}$$

As we see, mobility can be controlled in two different ways: either by changing the viscosity of the fluid (η) or by changing the distance between the plates in a Hele–Shaw cell (h). The first method leads to the viscous fingering phenomenon described in the preceding sections. The second method can be achieved by constructing a Hele–Shaw cell with a soluble bottom, as illustrated in Fig. 3.9a.

One possibility is to place a thin gypsum plate at the bottom of the Hele–Shaw cell. Since gypsum dissolves in water, a dissolved region forms near the inlet during the experiment (left-hand side in Fig. 3.9). The reaction front develops once all the soluble material at the inlet is dissolved and the distance between the plates (aperture) reaches a maximum, $h_{\max}$. This front advances into the matrix, as shown in Fig. 3.9b and c, which depict the front's position at a specific moment during the experiment. Upstream of the front, all soluble material has dissolved, resulting in a constant aperture, $h = h_{\max}$. Ahead of the front, the aperture gradually decreases to its initial value in the undissolved Hele–Shaw cell, $h = h_0$. The evolution of the dissolution patterns observed in such microfluidic experiments is illustrated in Fig. 3.10. As can be seen, the initially flat dissolution front soon breaks into fingers, which advance into the soluble substrate. We now describe this process quantitatively.

The flow in the system is still governed by the Poiseuille law (3.24), but the continuity equation becomes trickier to derive because the bottom plate dissolves, increasing the system volume. By integrating the incompressibility condition (3.13) over z, we obtain:

$$\frac{\partial q_x}{\partial x} + \frac{\partial q_y}{\partial y} + v_z(z_u) - v_z(z_l) = 0. \tag{3.83}$$

where $z_l(x, y)$ and $z_u(x, y)$ denote the positions of the lower and upper boundaries of the system at a given point, with $h = z_u - z_l$. Due to the no-slip boundary conditions for fluid motion at the walls, the last term on the LHS is simply $\frac{\partial h}{\partial t}$. Consequently, the continuity equation takes the form:

$$\nabla \cdot \boldsymbol{q} + \frac{\partial h}{\partial t} = 0, \tag{3.84}$$

again using the convention in which ∇ is a 2D operator acting in (x, y) plane.

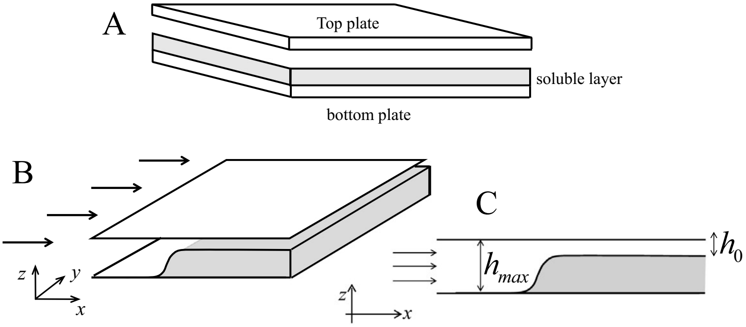

Fig. 3.9 Hele–Shaw cell with a soluble bottom (**a**). In the course of the experiment, a reactive fluid is injected from the left-hand side, dissolving the bottom layer (**b**). This process increases the aperture (h) and, consequently, the mobility in the dissolved region on the left compared to the undissolved region on the right (**c**)

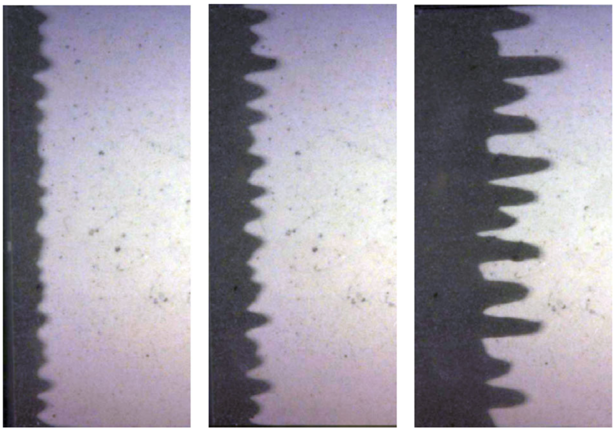

Fig. 3.10 Evolution of the dissolution patterns in the microfluidic experiments. The flow enters from the left and progressively dissolves the gypsum block. The front between the dissolved area (black) and the undissolved area (white) becomes unstable, leading to the formation of finger-like dissolution patterns

The next element needed for describing the dissolution process are the concentrations of chemical species within the system. These can be quite complex, with multiple components and nonlinear reaction rates. However, the dissolution of gypsum by water follows particularly simple kinetics (Colombani, 2008), which, to a good approximation, is linear in the undersaturation of calcium ions, Ca^{2+}. The dissolution rate (the number of dissolved molecules per unit area and unit time) is then

$$R(c) = r(c_{\text{sat}} - c)\theta(h_{\max} - h), \tag{3.85}$$

where c is the concentration of Ca^{2+} measured near the dissolving wall, i.e. at $z = z_l$, c_{sat} denotes the saturation concentration, at which the process stops, and r is the dissolution rate constant. The Heaviside step function $\theta(x)$ in (3.85) is defined as

$$\theta(x) = \begin{cases} 0 \text{ if } x \le 0 \\ 1 \text{ if } x > 0 \end{cases}. \tag{3.86}$$

In this way, dissolution is allowed only where there is still a soluble substance, i.e., for $h < h_{\max}$. A similar, product-controlled reaction kinetics as in (3.85) is also applicable to other minerals, such as halite (dissolved by water) or limestone dissolved by CO_2-saturated water (Plummer et al., 1978), at pH values similar to those of natural groundwater.

On the other hand, when limestone is dissolved by strong acids, as it is the case in the acidization of petroleum wells, the dissolution rate is controlled by the supply of reactant and becomes

$$R(c) = -rc\theta(h_{\max} - h), \tag{3.87}$$

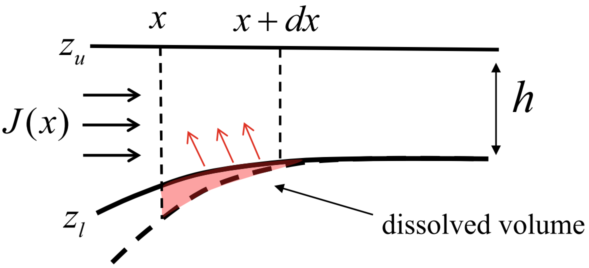

Fig. 3.11 The concentration balance in a dissolving fracture: Ca^{2+} ions are released during dissolution, causing the solution to saturate as it flows toward the outlet

where c is now the concentration of the H^+ ions. A different sign of (3.87) with respect to (3.85) reflects the fact that the reactant (H^+) is consumed during the reaction, whereas the concentration of the product (Ca^{2+}) increases.

Note that, from the perspective of reactive transport equations, the model (3.85) can be mapped onto (3.87) by the variable change, $c' = c_{\mathrm{sat}} - c$, which corresponds to tracking undersaturation. For simplicity, we will adopt the reaction law (3.87) below, keeping in mind that for the Hele–Shaw cell with a gypsum plate at the bottom, c should be interpreted as the undersaturation.

Let us now analyze the mass balance of the reactant in the system (Fig. 3.11). For simplicity, we temporarily focus on a two-dimensional (xz) case, assuming that the flow occurs along the x direction.

The total (z-integrated) reactant flux at a given point can be expressed as

$$J = \int_{z_l}^{z_u} \left(-D \frac{\partial c}{\partial x} + c v_x \right) dz. \tag{3.88}$$

There is a subtlety here that is usually glossed over in the literature (Balakotaiah, 2004). Namely, as we integrate over the vertical coordinate (z) in Eq. (3.88), we encounter two different averages of the concentration field. The first (diffusive) term leads to the standard (arithmetic) average over the aperture

$$c_{\mathrm{av}}(x, y) = \frac{1}{h} \int_{z_l}^{z_u} c(x, y, z) dz, \tag{3.89}$$

whereas the advective term leads to the so-called cup-mixing average

$$c_{\mathrm{cm}}(x, y) = \frac{1}{q} \int_{z_l}^{z_u} v_x(x, y, z) c(x, y, z) dz. \tag{3.90}$$

This represents the concentration that would be measured in a cup collecting liquid from a specific cross-section (x) of the system. Naturally, regions with higher flow velocities contribute more liquid to the cup, leading to the flow-weighted average in Eq. (3.90). Using these two averages, the concentration volumetric flux (3.88) can be expressed as

$$J = -Dh\frac{\partial c_{\text{av}}}{\partial x} + q_x c_{\text{cm}}. \tag{3.91}$$

We now analyze concentration mass balance in a small volume of a system in between x and $x + dx$, delineated by dashed lines in Fig. 3.11. The incoming and outgoing fluxes into this volume are $J(x)$ and $J(x + dx)$, respectively. Additionally, ions are generated along the boundary due to dissolution, with their production rate (per unit time) given by $R(c_{\text{wall}})ds$, where c_{wall} is the concentration at the wall and ds is the arclength element. The total change of the number of ions in this volume can thus be expressed in terms of the flux as

$$\Delta N = N(t + dt) - N(t) = \Big[c_{\text{av}}(t + dt)h(t + dt) - c_{\text{av}}(t)h(t)\Big]dx =$$

$$dt\Big[J(x) - J(x + dx) + R(c_{\text{wall}})ds\Big]. \tag{3.92}$$

Using (3.87) and (3.91), and then taking the limit $dt \to 0,\ dx \to 0$, we obtain

$$\frac{\partial(hc_{\text{av}})}{\partial t} + \frac{\partial}{\partial x}(c_{\text{cm}}q_x) = \frac{\partial}{\partial x}Dh\frac{\partial(c_{\text{av}})}{\partial x} - rc_{\text{wall}}\theta(h_{\max} - h)\sqrt{1 + \left(\frac{dh}{dx}\right)^2}. \tag{3.93}$$

Here, the geometric factor $\sqrt{1 + (\frac{dh}{dx})^2}$ represents $\frac{ds}{dx}$. Generalizing the transport equation to two spatial dimensions (x and y) we obtain

$$\frac{\partial(hc_{\text{av}})}{\partial t} + \nabla \cdot (c_{\text{cm}}\boldsymbol{q}) = \nabla \cdot \Big(Dh\nabla c_{\text{av}}\Big) - rc_{\text{wall}}\sqrt{1 + (|\nabla h|)^2}\theta(h_{\max} - h). \tag{3.94}$$

Finally, the erosion equation, describing the growth of the aperture due to the dissolution of the gypsum plate at the bottom, is given by:

$$(1 - \varphi)\partial_t h = \chi\nu rc_{\text{wall}}\sqrt{1 + (|\nabla h|)^2}\theta(h_{\max} - h), \tag{3.95}$$

where the factor $(1 - \varphi)$ accounts for the fraction of the gypsum crystals in a unit volume of the dissolving material, with φ representing its porosity (in the experiments of Fig. 3.10, $\varphi \approx 0.5$). Next, ν is the molar volume of the solid species, and χ accounts for the stoichiometry of the reaction. The geometric factor, $\sqrt{1 + (|\nabla h|)^2}$ appears again, this time linking the normal growth rate with the growth rate along the vertical direction (z).

The flow and transport equations must be supplemented by the boundary conditions that reflect the physical setup in which the fracture is dissolved by a fluid with reactant concentration c_{in} which infiltrates the system, entering from the left-hand side with a flow rate q_0, i.e.

$$\lim_{x\to-\infty} \boldsymbol{q} = q_0 \hat{\boldsymbol{e}}_x, \tag{3.96}$$

$$\lim_{x\to-\infty} c = c_{in}. \tag{3.97}$$

We should keep in mind that—since in the case of gypsum dissolution c stands for the undersaturation, the condition $c = c_{in} > 0$ means that the incoming water is undersaturated with respect to calcium ions, $c_{\mathrm{Ca}^{2+}} < c^{sat}_{\mathrm{Ca}^{2+}}$. In the experiment shown in Fig. 3.10, the incoming fluid is pure water, so in this case, $c_{\mathrm{Ca}^{2+}} = 0$ and thus $c_{in} = c^{sat}_{\mathrm{Ca}^{2+}}$.

The corresponding boundary conditions at $x \to +\infty$ are:

$$\lim_{x\to\infty} \boldsymbol{q} = q_0 \hat{\boldsymbol{e}}_x, \tag{3.98}$$

$$\lim_{x\to\infty} c = 0. \tag{3.99}$$

From now on, we will make a number of assumptions that will allow us to keep the exposition simple. First, we will ignore the geometric factor, $\sqrt{1 + (|\nabla h|)^2}$, assuming that the aperture gradients are relatively small, $|\nabla h| \ll 1$. Second, we will assume that the diffusion along the z-direction is fast enough so that all three different concentrations appearing in (3.95) can be considered equal; $c_{\mathrm{wall}} = c_{\mathrm{av}} = c_{cm}$. This assumption can be relaxed (Szymczak & Ladd, 2012), but at the cost of additional mathematical complexity.

3.7 Small Acid Capacity Limit

> Constantly secretly eating its way,
> The acid is making the substance its prey …
>
> —Thomas Hood *Etching Moralized*

The various factors that appear together in the erosion equation (3.95) can be grouped into the so-called acid capacity number $\gamma_a = \frac{\chi c_{in} \nu}{1-\varphi}$. This parameter is defined as the ratio of the volume of soluble rock (of molar volume ν and porosity φ) to the volume of incoming fluid required to dissolve it completely.

In typical geophysical systems, the reactant is dilute ($c_{in} \ll \nu^{-1}$), resulting in $\gamma_a \ll 1$. For instance, when calcite is dissolved by aqueous CO_2, $\gamma_a \sim 10^{-4}$. When $\gamma_a \ll 1$, the velocity and concentration fields reach a steady state long before any significant changes occur in the aperture field. This can be formalized through the following change of coordinates and rescaling of the fields:

$$t' = t/t_0, \qquad x' = x/h_0, \qquad y' = y/h_0 \tag{3.100}$$

$$c' = c/c_{in}, \qquad \boldsymbol{q}' = \boldsymbol{q}/q_0, \quad h' = h/h_0 \quad p' = p h_0^2/(12\eta q_0), \tag{3.101}$$

where h_0 is the initial average aperture in the fracture, and q_0 is a characteristic flow rate. For example, in the case of a Hele–Shaw cell supplied with a total volumetric flux Q of solution, the natural choice for q_0 is $q_0 = Q/W$, where W is the width of the system.

The timescale t_0 introduced above is defined as

$$t_0 = \frac{h_0}{\gamma_a r} \tag{3.102}$$

which corresponds to the characteristic time required for the aperture at the inlet (initially h_0) to double as a result of dissolution.

In these variables, the equations take the following form:

$$\gamma_a \mathrm{Da} \frac{\partial h'}{\partial t'} + \nabla' \cdot \boldsymbol{q}' = 0 \tag{3.103}$$

$$\gamma_a \mathrm{Da} \frac{\partial (h'c')}{\partial t'} + \nabla' \cdot (c'\boldsymbol{q}') = \frac{1}{\mathrm{Pe}} \nabla \cdot (h'\nabla c') - \mathrm{Da} c' \theta(h'_{\max} - h') \tag{3.104}$$

$$\frac{\partial h'}{\partial t'} = c'\theta(h'_{\max} - h') \tag{3.105}$$

where the two dimensionless numbers appear: the Damköhler number:

$$\mathrm{Da} = \frac{r h_0}{q_0}, \tag{3.106}$$

and the Péclet number

$$\mathrm{Pe} = \frac{q_0}{D}. \tag{3.107}$$

The Damköhler number quantifies the relative magnitudes of reactive and advective effects, whereas the Péclet number represents the ratio of advection to diffusion in the system.

In the limit $\gamma_a \to 0$, the flow and transport equations become stationary and are given by (Ladd & Szymczak, 2017):

$$\boldsymbol{q}' = (h')^3 \nabla' p', \qquad \nabla' \cdot \boldsymbol{q}' = 0, \tag{3.108}$$

$$\nabla' \cdot (c'\boldsymbol{q}') = \frac{1}{\mathrm{Pe}} \nabla \cdot (h'\nabla c') - \mathrm{Da} c' \theta(h'_{\max} - h'), \tag{3.109}$$

whereas the last equation describes the evolution of the aperture over a longer timescale

$$\frac{\partial h'}{\partial t'} = c'\theta(h'_{\max} - h'). \tag{3.110}$$

This is the limit we adopt from now on.

3.8 Upstream and Downstream Penetration Length

> I live upstream, you live downstream,
> Day after day I long for you.
> We drink from the same river's stream,
> Yet you are never in my view.
>
> —Li Zhiyi *Song of Divination*

Let us for a moment consider a situation in which the reaction front is planar, i.e., the region $x < x_f(t)$ is completely dissolved ($h(x) = h_{\max}$). In this case, the flow is uniform, $\boldsymbol{q} = q_0\hat{\boldsymbol{e}}_x$, and the transport equation reduces to the 1D form:

$$\frac{dc'}{dx'} = \frac{1}{\mathrm{Pe}}\frac{\partial}{\partial x'}(h'\frac{dc'}{dx'}) - \mathrm{Da}c'\theta(h' - h'_{\max}) \tag{3.111}$$

which has the following solution in the region $x' < x'_f$, where the reaction term vanishes (since $h = h_{\max}$ there):

$$c(x) = 1 - A\exp\left((x' - x'_f)/l'_u\right), \quad x' < x'_f, \tag{3.112}$$

where l'_u is the upstream penetration length

$$l'_u = \frac{h'_{\max}}{\mathrm{Pe}}. \tag{3.113}$$

The solution downstream is more complicated, as the aperture is generally a function of x in that region. However, for large x, where $h(x) \to h_0$, we obtain the following asymptotic behavior:

$$c(x) = Be^{-(x'-x'_f)/l'_d}, \quad x \to \infty \tag{3.114}$$

with the downstream penetration length of the form

$$l'_d = \frac{\sqrt{1 + 4\frac{\mathrm{Da}}{\mathrm{Pe}}} + 1}{2\mathrm{Da}}, \tag{3.115}$$

as illustrated in Fig. 3.12. The upstream penetration length is of a diffusive character, whereas the downstream length is determined by the interplay of transport and reaction.

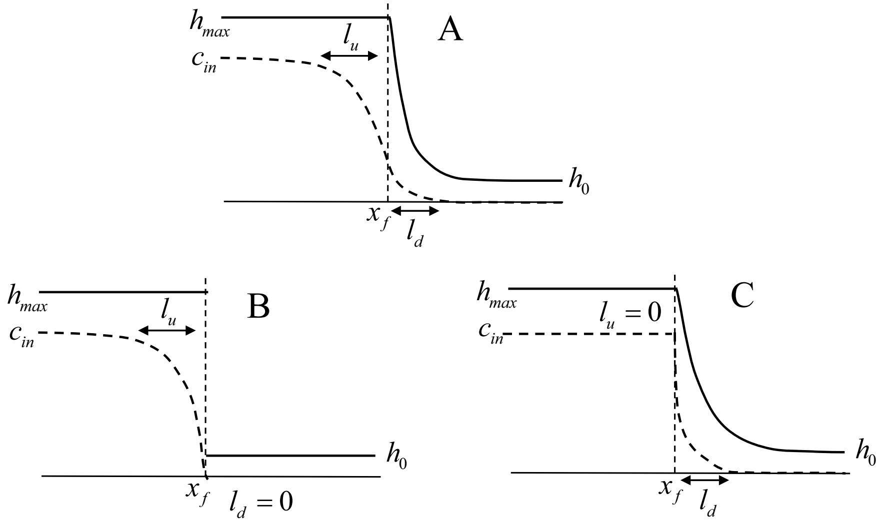

Fig. 3.12 Concentration (dashed lines) and aperture (solid) profiles. **a** The concentration profile decays with different length scales, l_u and l_d, in the upstream ($x < x_f(t)$) and downstream ($x > x_f(t)$) regions, with $x_f(t)$ marking the position of a reaction front. **b** The thin-front limit, dominated by diffusion in the upstream region, in which $l_u \gg l_d$. **c** The convection-dominated regime in which $l_d \gg l_u$

3.9 Thin Front Limit

> Stern, threatening, inaccessible, and intangible
> line which separates two hostile armies was
> all the more clearly felt.
>
> —Leo Tolstoy *War and Peace*

The ratio of the downstream and upstream penetration lengths

$$l_d/l_u = \frac{h_0}{h_{\max}} \frac{\sqrt{1+4H}+1}{2H} = \frac{h_0}{h_{\max}} \frac{2}{\sqrt{1+4H}-1} \tag{3.116}$$

is determined by the parameter

$$H = \frac{\mathrm{Da}}{\mathrm{Pe}} = \frac{rDh_0}{q_0^2}. \tag{3.117}$$

In particular

$$l_u/l_d \to 0 \qquad \text{as } H \to 0 \tag{3.118}$$

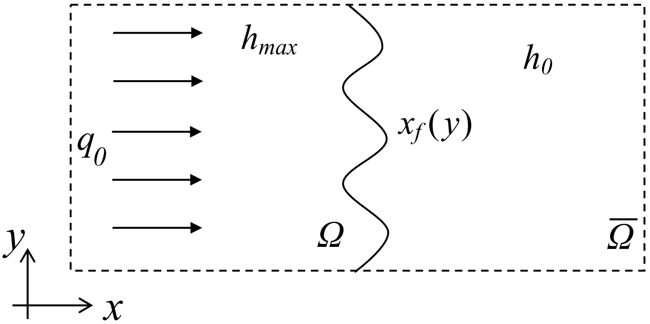

Fig. 3.13 Geometry of the system: a reactive fluid is injected from the left side and dissolves the fracture through chemical reactions. As dissolution progresses, the reaction front, $x_f(y)$ (shown by the solid line), advances into the matrix, separating the fully dissolved, upstream domain (Ω) with aperture $h_{\max}$ from the undissolved part of the fracture with initial aperture h_0

defines the so-called convection dominated regime (Fig. 3.12c). In this regime, diffusion in the upstream region can be neglected, and the solution $c = c_{in}$ can be used there. All the interesting dynamics then occur in the partially dissolved region downstream, with the penetration length controlled solely by convection:

$$l_d = \frac{q}{r}. \tag{3.119}$$

On the other hand, the opposite case

$$l_d/l_u \to 0 \quad \text{as} \quad H \to \infty \tag{3.120}$$

defines the so-called thin-front limit, dominated by diffusion in the upstream region, with the downstream reactive length negligible in comparison to the upstream diffusive length (Chadam et al., 1986; Ortoleva et al., 1987; Szymczak & Ladd, 2013; Kondratiuk & Szymczak, 2015). In this limit, one can assume that the reaction occurs instantaneously, with the reactants fully consumed at the dissolution front, as shown in Fig. 3.12b. This is the limit we will consider from now on due to its relative simplicity. A more detailed discussion of the small acid capacity limit, thin-front limit, and their applicability to physical problems can be found in Ladd and Szymczak (2017).

In the thin-front limit, we obtain a Muskat-like problem in which the space is divided into two domains: the dissolved upstream domain (Ω) with aperture $h_{\max}$ and the undissolved downstream domain ($\bar{\Omega}$) with aperture h_0, complementary to Ω (*cf.* Fig. 3.13). However, the system is more complex than the standard Muskat problem of Fig. 3.2 due to the presence of the concentration field. In particular, the advancement of the boundary between the phases is no longer directly linked to the flow field, as was the case for viscous fingering, but rather to the flux of the reactant at a given point

$$U_n = \bar{\boldsymbol{n}} \cdot \frac{d\boldsymbol{r}_f}{dt} = -\frac{\chi\nu}{(1-\varphi)(h_{\max}-h_0)} D h_{\max} (\nabla c)_n = \\ -\frac{\gamma_a}{c_{in}(h_{\max}-h_0)} D h_{\max} (\nabla c)_n \qquad \boldsymbol{r} \in \partial\Omega(t). \tag{3.121}$$

Only the diffusive flux $J = -Dh_{\max}\nabla c$ is present in Eq. (3.121), since the concentration at the front vanishes, and so does the convective contribution to the flux. The front velocity (3.121) is then obtained from the flux by observing that the total volume dissolved by the reactant particles crossing the reaction front over time Δt can be expressed, on one hand, as $\chi\nu J\Delta t$, and, on the other, as $(1-\varphi)U\Delta t(h_{\max}-h_0)$ (see Fig. 3.14).

Since the aperture in each domain (Ω and $\bar{\Omega}$) is constant, the pressure obeys the Laplace equation in both domains

$$\nabla^2 p_1 = 0, \qquad \nabla^2 p_2 = 0, \tag{3.122}$$

whereas the concentration field is governed by the convection-diffusion equation

$$\nabla \cdot (\boldsymbol{q} c_1) - D h_{\max} \nabla \cdot (D \cdot \nabla c_1) = 0 \tag{3.123}$$

in the upstream region (Ω). In the downstream region, $c_2 = 0$. Additionally, both the pressure and the normal component of the fluid flux need to be continuous across the reaction front $\partial\Omega$:

$$p_1|_{x_f(y)} = p_2|_{x_f(y)}, \tag{3.124}$$

$$q_{1n}|_{x_f(y)} = q_{2n}|_{x_f(y)} \tag{3.125}$$

and we need to obey the boundary conditions (3.96)–(3.99).

The uniform, y-independent solutions of equations (3.122) with these boundary conditions are

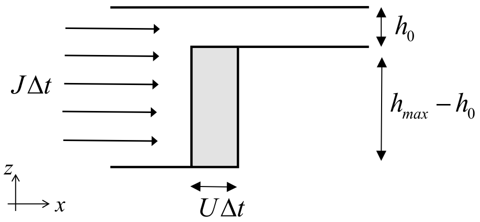

Fig. 3.14 Cross-section of the system in xz plane in the thin-front limit. Over the time interval Δt, $J\Delta t$ molecules of the reactant (per unit length in the y direction) dissolve an area of $\chi\nu J\Delta t$ of the mineral (marked in grey in the Figure), which can also be expressed as $(1-\varphi)(h_{\max}-h_0)U\Delta t$. The comparison of both expression for the dissolved volume leads to Eq. (3.121)

$$p_1^0 = -\tfrac{q_0}{M_1}(x - U_0 t), \tag{3.126}$$

$$p_2^0 = -\tfrac{q_0}{M_2}(x - U_0 t), \tag{3.127}$$

$$\boldsymbol{q}_1^0 = \boldsymbol{q}_2^0 = q_0 \hat{\boldsymbol{e}}_x, \tag{3.128}$$

where M_1 and M_2 are the mobilities of the upstream (downstream) domain and we assumed that initially the front was positioned at $x = 0$, i.e. $x_f^0(t = 0) = 0$. The additive constant in the pressure has been chosen in such a way that p vanishes at the reaction front. As we see, the front moves with a constant velocity, U_0, with $x_f^0(t) = U_0 t$.

The concentration profile is then of the form:

$$c^0 = c_{in}(1 - \mathrm{e}^{\frac{x - x_f^0(t)}{l_u}}), \quad x < x_f^0 \tag{3.129}$$

with the diffusive length $l_u = D h_{\max}/q_0$. Eqs. (3.121), (3.129) and (3.113) give the front velocity of the form

$$U_0 = \frac{\gamma_a}{h_{\max} - h_0} q_0, \tag{3.130}$$

which can also be directly deduced from the mass conservation.

3.10 Linear Stability Analysis

> Things fall apart; the centre cannot hold;
> Mere anarchy is loosed upon the world
>
> —W. B. Yeats *The Second Coming*

Similarly to the case of viscous fingering, let us now introduce infinitesimal perturbations of the front position as well as in the pressure, velocity and concentration fields

$$x_f \longrightarrow x_f^0 + \delta x_f, \tag{3.131}$$

$$p_1 \longrightarrow p_1^0 + \delta p_1, \tag{3.132}$$

$$\boldsymbol{q}_1 \longrightarrow q_0 \hat{\boldsymbol{e}}_x + \delta \boldsymbol{q}_1, \tag{3.133}$$

$$c_1 \longrightarrow c^0 + \delta c_1, \tag{3.134}$$

and analogously for the downstream part. This form of the solutions is then inserted into the flow and transport equations, neglecting the terms of the order higher than linear. Again, due to the linearity of the equations, we will consider individual Fourier components, e.g.

$$\delta x_f = \varepsilon \mathrm{e}^{\sigma t} \sin(ky). \tag{3.135}$$

The pressure perturbation obeys the Laplace equation

$$\Delta\delta p = 0 \tag{3.136}$$

from which the flow perturbation can then be calculated as

$$\boldsymbol{\delta q} = -M\nabla\delta p, \tag{3.137}$$

with the boundary conditions

$$\lim_{x\to-\infty} \delta\boldsymbol{q}_1 = 0, \tag{3.138}$$

$$\lim_{x\to\infty} \delta\boldsymbol{q}_2 = 0, \tag{3.139}$$

$$\left(p_1^0 - p_2^0\right)_{x_f^0} + \left(\delta p_1 - \delta p_2\right)_{x_f^0} + \delta x_f\left(\frac{\partial p_1^0}{\partial x} - \frac{\partial p_2^0}{\partial x}\right)_{x_f^0} = 0, \tag{3.140}$$

$$\delta q_{1n}\Big|_{x_f^0} = \delta q_{2n}\Big|_{x_f^0}. \tag{3.141}$$

The first two relations are the requirements that the perturbations vanish far away from the front. The last two are obtained by linearizing the continuity condition, (3.124)–(3.125) at the perturbed front. Similarly to the viscous fingering case, we will find it more convenient to work in the moving front coordinates, $\bar{x} = x - x_f^0 = x - U_0 t$. The good news is that, since the pressure perturbations are the solutions to the Laplace equation, they have the same form as derived before (3.47)

$$\delta p_1 = \delta A_1 \sin(ky)\exp(k\bar{x}), \tag{3.142}$$

$$\delta p_2 = \delta A_2 \sin(ky)\exp(-k\bar{x}), \tag{3.143}$$

where the relation between δA_1 and δA_2 is obtained from the pressure continuity (analogously to Eq. (3.54) but without the surface tension):

$$\left(\delta A_1 - \delta A_2\right) + \varepsilon\left(-\frac{q_0}{M_1} + \frac{q_0}{M_2}\right) = 0 \tag{3.144}$$

and from the continuity of the normal component of the fluid flux (q_n), which gives (cf. Eq. 3.65)

$$\delta A_1 M_1 = -\delta A_2 M_2. \tag{3.145}$$

This finally leads to

$$\delta A_1 = -\frac{\varepsilon q_0 (M_1 - M_2)}{M_1(M_1 + M_2)} \tag{3.146}$$

in full analogy to Eq. (3.66). The pressure perturbations are thus

$$\delta p_1 = -\varepsilon \mathrm{e}^{\sigma t} q_0 \frac{M_1 - M_2}{M_1 + M_2} \frac{1}{M_1} \sin(ky) \mathrm{e}^{k\bar{x}}, \tag{3.147}$$

$$\delta p_2 = \varepsilon \mathrm{e}^{\sigma t} q_0 \frac{M_1 - M_2}{M_1 + M_2} \frac{1}{M_2} \sin(ky) \mathrm{e}^{-k\bar{x}}. \tag{3.148}$$

The Darcy law can now be used to calculate $\boldsymbol{q}_1$:

$$\boldsymbol{q}_1 = q_0 \hat{\boldsymbol{e}}_x + \varepsilon \mathrm{e}^{\sigma t} q_0 \frac{M_1 - M_2}{M_1 + M_2} k \mathrm{e}^{k\bar{x}} (\sin(ky) \hat{\boldsymbol{e}}_x + \cos(ky) \hat{\boldsymbol{e}}_y), \tag{3.149}$$

where the second term corresponds to the perturbation, $\delta \boldsymbol{q}_1$.

Next, we solve for the concentration perturbation. The transport equation takes the form:

$$Dh_{\max} \nabla^2 c = q_0 \frac{\partial c}{\partial \bar{x}} + \delta q_{1x} \frac{\partial c}{\partial \bar{x}} + \delta q_{1y} \frac{\partial c}{\partial y}, \tag{3.150}$$

where we now need to insert $c = c^0 + \delta c$ and keep only linear terms in perturbations. This leads to

$$Dh_{\max} \nabla^2 \delta c = q_0 \frac{\partial \delta c}{\partial \bar{x}} + \delta q_{1x} \frac{\partial c^0}{\partial \bar{x}}. \tag{3.151}$$

Since the concentration perturbation will be of the form

$$\delta c = \delta C(\bar{x}, t) \sin(ky), \tag{3.152}$$

then $\nabla^2 \delta c = (\delta C'' - k^2 \delta C) \sin(ky)$ with prime standing for differentiation with respect to x. Inserting this, alongside (3.149), into (3.151) and using the fact that $\frac{\partial c^0}{\partial \bar{x}} = -\frac{c_{in} q_0}{Dh_{\max}} e^{\frac{q_0}{Dh_{\max}} \bar{x}}$ leads finally to

$$\frac{Dh_{\max}}{q_0} (\delta C'' - k^2 \delta C) = \delta C' - \varepsilon k e^{k\bar{x}} \frac{c_{in} q_0}{Dh_{\max}} \frac{M_1 - M_2}{M_1 + M_2} e^{\frac{q_0}{Dh_{\max}} \bar{x}}. \tag{3.153}$$

This is an inhomogeneous equation for $\delta C(\bar{x})$. The homogeneous one (obtained after dropping the last term in (3.153)) is solved by an exponential function $E e^{\lambda_+ \bar{x}}$ with

$$\lambda_+ = \frac{q_0}{2Dh_{\max}} \left(1 + \sqrt{1 + 4 \left(\frac{k Dh_{\max}}{q_0} \right)^2} \right), \tag{3.154}$$

where we take the root that gives the solution decaying at $-\infty$. Additionally, we can easily check that $-\varepsilon \frac{c_{in} q_0}{Dh_{\max}} \frac{M_1 - M_2}{M_1 + M_2} e^{(k + \frac{q_0}{Dh_{\max}}) \bar{x}}$ is a particular solution of the full, inhomogeneous equation. Finally

$$\delta c = E \mathrm{e}^{\lambda_+ \bar{x}} \sin(ky) - \varepsilon \frac{c_{in} q_0}{Dh_{\max}} \frac{M_1 - M_2}{M_1 + M_2} e^{(k + \frac{q_0}{Dh_{\max}}) \bar{x}} \sin(ky). \tag{3.155}$$

In order to determine E, we need to impose the boundary condition $c(\bar{x}_f) = 0$, which can be expanded to yield

$$(c^0 + \delta c)|_{\bar{x}_f^0 + \delta \bar{x}_f} = 0. \tag{3.156}$$

Up to quadratic terms, this becomes

$$\varepsilon \frac{\partial c^0}{\partial \bar{x}}|_{\bar{x}_f^0} = -\delta c(\bar{x}_f^0). \tag{3.157}$$

Substituting (3.129) and (3.155) into the above, and remembering that $\bar{x}_f^0 = 0$ in the moving frame, we get

$$-\varepsilon c_{in} \frac{q_0}{Dh_{\max}} = -\varepsilon \frac{c_{in} q_0}{Dh_{\max}} \frac{M_1 - M_2}{M_1 + M_2} + E. \tag{3.158}$$

Solving for E, we obtain

$$E = \varepsilon \frac{c_{in} q_0}{Dh_{\max}} \frac{2M_1}{M_1 + M_2}. \tag{3.159}$$

Finally, the growth rate of the perturbations can be obtained using the formula (3.121) for the front velocity

$$\boldsymbol{n} \cdot \frac{d\boldsymbol{r}_f}{dt} = -\frac{\gamma_a}{c_{in}(h_{\max} - h_0)} Dh_{\max} (\nabla c)_{\boldsymbol{r}_f} \cdot \boldsymbol{n}. \tag{3.160}$$

However, similarly to what we have shown for viscous fingering

$$\boldsymbol{n} = \hat{\boldsymbol{e}}_x + O(\varepsilon)\hat{\boldsymbol{e}}_y, \tag{3.161}$$

so it is sufficient to consider only the x component. Expanding (3.160) leads to

$$\frac{\partial \delta \bar{x}_f}{\partial t} = -\frac{Dh_{\max}\gamma_a}{c_{in}(h_{\max} - h_0)} \left(\delta \bar{x}_f \frac{\partial^2 c^0}{\partial \bar{x}^2}\bigg|_{\bar{x}_f^0} + \frac{\partial \delta c}{\partial \bar{x}}\bigg|_{\bar{x}_f^0} \right). \tag{3.162}$$

Finally, substituting (3.129) and (3.155) we obtain the dispersion relation of the form

$$\sigma(k) = \frac{U_0}{l_u(1 + \Gamma)} \left[(1 - \Gamma) k l_u + 1 - \sqrt{1 + 4(k l_u)^2} \right], \tag{3.163}$$

where, as before, $\Gamma = \frac{M_2}{M_1}$. As expected, the natural lengthscale for this problem is the upstream penetration length, $l_u = \frac{Dh_{\max}}{q_0}$, whereas the natural timescale is $\tau = l_u / U_0$, i.e. the time over which the dissolution front moves over the length l_u. Scaling time by τ and spatial variables by l_u gives finally

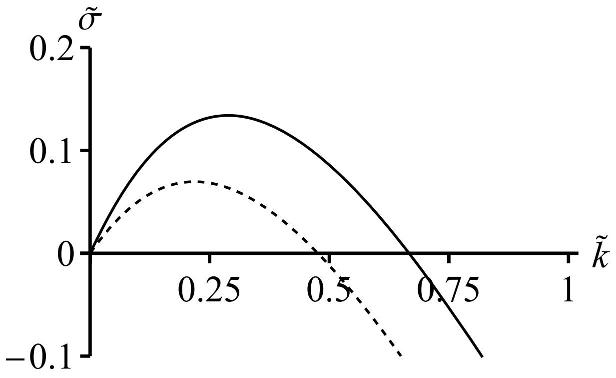

Fig. 3.15 Dispersion relation for reactive-infiltration instability given by Eq. (3.164) for mobility ratio $\Gamma = 0$ (solid line) and $\Gamma = 0.2$ (dashed line)

$$\tilde{\sigma}(\tilde{k}) = \frac{1}{1+\Gamma}\left[(1-\Gamma)\tilde{k} + 1 - \sqrt{1+4\tilde{k}^2}\right]. \tag{3.164}$$

with $\tilde{k} = kl_u$. and $\tilde{\sigma} = \tau\sigma$.

Figure 3.15 shows the dispersion relation given by (3.164). For long wavelengths (small k) the dependence of the growth rate on the wave vector is linear

$$\tilde{\sigma}(\tilde{k}) \approx \frac{1-\Gamma}{1+\Gamma}\tilde{k} = \frac{M_1 - M_2}{M_1 + M_2}\tilde{k} \tag{3.165}$$

with a coefficient that depends on the mobility contrast between the phases. Since K is an increasing function of porosity, and dissolution results in porosity increase, we infer that $M_1 > M_2$, thus $\tilde{\sigma}(\tilde{k}) > 0$ in small $\tilde{k}$ region. Note that relation (3.165) remains in agreement with the analogous formula (3.73) for the Saffman–Taylor (viscous fingering) instability.

On the other hand, for large $\tilde{k}$, the dominating term in (3.164) is negative, and the perturbations become stabilized by diffusion. The largest unstable wavevector (corresponding to the shortest unstable wavelength) is given by

$$\tilde{k}_0 = \frac{2(1-\Gamma)}{4-(1-\Gamma)^2}. \tag{3.166}$$

The maximum of the dispersion relation corresponds to

$$\tilde{k}_c = \frac{1-\Gamma}{2\sqrt{4-(1-\Gamma)^2}}, \tag{3.167}$$

which determines the wavelength $\lambda_c = 2\pi D h_{\max}/\tilde{k}_c q_0$ of the most unstable mode. As we see, for larger flow rates the instability wavelength decreases, which is again a feature analogous to that of the Saffman–Taylor instability.

3.11 Hele–Shaw Cell Versus Porous Media

> The stone,
> Hard as it is, in every winding pore
> Holds multitudes.
>
> James Thomson *The Seasons*

So far, we have formulated our results for the Hele–Shaw cell with a soluble bottom. However, the governing equations for this system are in close analogy to the equations of dissolving porous media, as summarized below:

Fractures	**Porous media**
aperture (h)	porosity (φ)
$\boldsymbol{q} = -\frac{h^3}{12\eta}\nabla p(x, y);$	$\boldsymbol{u} = -\frac{K(\varphi)}{\eta}\nabla p;$
$\nabla \cdot \boldsymbol{q} = 0;$	$\nabla \cdot \boldsymbol{u} = 0;$
$\nabla \cdot (\boldsymbol{q}c) - \nabla \cdot (hD\nabla c) = -rc$	$\nabla \cdot (\boldsymbol{u}c) - \nabla \cdot (\varphi \boldsymbol{D}\nabla c) = -rs(\varphi)c$
$\nabla \cdot \boldsymbol{q} = 0;$	$\nabla \cdot \boldsymbol{u} = 0;$
$\mathrm{Da} = \frac{rh_0}{q_0}$	$\mathrm{Da} = \frac{r}{u_0}$
$\mathrm{Pe} = \frac{q_0}{D}.$	$\mathrm{Pe} = \frac{u_0}{Ds\varphi_0}.$

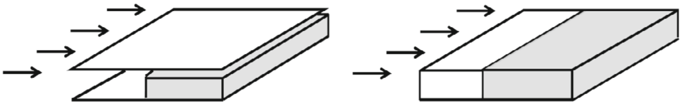

(3.168)

As we see, in the porous media, the role equivalent to the aperture, h, is played by porosity, φ, which is the fraction of the void space in a given place of a porous material. Next, the equivalent of $\boldsymbol{q}$ is the Darcy velocity, $\boldsymbol{u}$, which quantifies the volume of water that flows through a unit cross-sectional area of a porous medium per unit time. The Darcy velocity is connected to the average fluid velocity in the pores, $\boldsymbol{v}$, by $\boldsymbol{u} = \varphi \boldsymbol{v}$ (since only a portion of the space is available for the water flow) and it is connected with the pressure gradient by the Darcy law

$$\boldsymbol{u} = -\frac{K(\varphi)}{\eta} \nabla p, \tag{3.169}$$

where K is the so-called permeability, which is the function of geometry of the pore-space, generally increasing with porosity.

Additionally, in the porous media equations the molecular diffusion coefficient, D, is replaced by the tensor $\boldsymbol{D}(\varphi, \boldsymbol{u})$, quantifying dispersion in the porous medium, which will generally depend on both porosity and flow rate. Finally, since the reaction takes place at pore surfaces, we need to provide the specific surface area, $s(\varphi)$, which is defined as the total area of a dissolving mineral per unit volume. We note in passing that a precise estimate of $s(\varphi)$ for a particular rock type is a challenging task, requiring a careful experimental analysis (Noiriel et al., 2009).

Finally, Eq. (3.168) shows the relevant definitions of the Péclet and Damköhler numbers for the porous media case, with u_0 standing for the average Darcy velocity in the system and φ_0 for the initial porosity.

Using the above analogy, we can repeat our considerations for porous materials, obtaining—again in the thin front limit—a relation analogous to (3.163)

$$\sigma(k) = \frac{U_0}{l_u(1+\Gamma)} \left[(1-\Gamma)kl_u + 1 - \sqrt{1 + 4(kl_u)^2} \right]. \tag{3.170}$$

but this time with

$$l_u = \frac{D\varphi_{\max}}{u_0} \tag{3.171}$$

and

$$U_0 = \frac{\gamma_a}{\varphi_{\max} - \varphi_0} u_0, \tag{3.172}$$

where $\varphi_{\max}$ is the porosity of the fully dissolved medium. If the rock is fully soluble, then $\varphi_{\max} = 1$, however in the presence of insoluble matrix, $\varphi_{\max} = 1 - \varphi_{\text{ins}}$, where φ_{ins} is the volume fraction of the insoluble component.

For porous media, relation (3.170) was first derived by Chadam et al. (1986).

The results of the linear stability analysis in Sect. 3.10 were established in the thin-front limit ($H \to \infty$). This limit is particularly simple, as all the reactant is consumed at the front, and there is no need to resolve the concentration field downstream. A more general case for any H can be considered, but it comes at the cost of increased mathematical complexity. For further details, we refer the reader to Szymczak and Ladd (2013); here, we will focus on the general conclusions from these considerations.

First, in dissolution problems, as we previously noted, there are two characteristic length scales, l_d and l_u. Generally, the instability selects the longer of these scales:

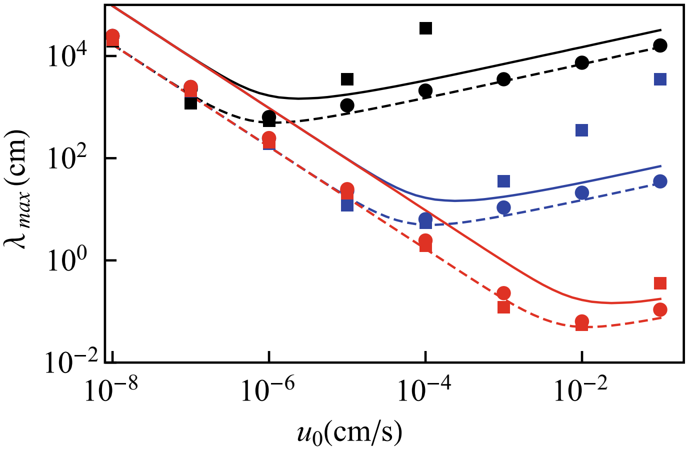

Fig. 3.16 The maximally unstable wavelength for different products of reaction rate and specific reactive area: $rs = 10^{-8}\,\mathrm{s}^{-1}$ (black), $rs = 10^{-4}\,\mathrm{s}^{-1}$ (blue), and $rs = 1\,\mathrm{s}^{-1}$ (red) (Szymczak & Ladd, 2013). For each reaction rate, results are shown for three different porosity contrasts: $\Delta = 0.1$ (solid line), $\Delta = 1$ (dashed line and circles), and $\Delta = 10$ (squares), which correspond to the mobility ratios $\Gamma = 0.75, 0.125$ and 7.5×10^{-4}, respectively. Analytic results derived by Szymczak and Ladd (2013) in the small porosity contrast limit are shown by lines, and numerical results are represented by solid symbols

for $H \to \infty$, this will be l_u, whereas for $H \to 0$, the downstream penetration length, l_d, takes on this role. Importantly, these length scales depend differently on the flow rate: l_u decreases with u, while l_d increases.

Figure 3.16 shows the fastest-growing wavelength of reactive-infiltration instability for a system with fixed r, s, and D, and variable flow rate (u_0), ranging from 10^{-8} to 10^{-1} cm/s. The lower end of the scale covers naturally occurring flow rates in subsurface systems, while much higher velocities (up to 0.1 cm/s) are typical of reservoir acidization in the petroleum industry. Results are shown for three different reaction time scales: $(rs)^{-1} = 10^8$ s, which is characteristic of slowly dissolving minerals such as quartz and certain redox reactions, $(rs)^{-1} = 10^4$ s, typical of the dissolution of clays, and $(rs)^{-1} = 1$ s, characteristic of fast-dissolving minerals such as calcite or gypsum. We assume here a constant diffusion coefficient, $D = 10^{-5}\,\mathrm{cm}^2/\mathrm{s}$.

The results in Fig. 3.16 are presented for three different values of the mobility ratio. Knowing the relationship between mobility and porosity, these values can be linked to the corresponding normalized porosity contrast between the dissolved and undissolved phases:

$$\Delta = \frac{\varphi_{\max} - \varphi_0}{\varphi_0}. \tag{3.173}$$

In Szymczak and Ladd (2013), the relationship $M(\varphi)$ was assumed to take the form $M(\varphi) = M_0\varphi^3$, thus the corresponding mobility ratio is then $\Gamma = (1 + \Delta)^{-3}$.

Figure 3.16 shows that there is a lower bound to the wavelength with respect to the flow velocity. Starting from the thin-front limit ($u_0 \sim 10^{-8}$ cm/s), increasing velocity reduces the wavelength by decreasing the upstream penetration length, $l_u = D\varphi_{\max}/u_0$; in this region ($H \gg 1$) the downstream penetration length is small. However, as u_0 increases further, the downstream length begins to grow, and when $H < 1$, it takes over as the dominant scale. In this case, an increase in velocity leads to an increase in penetration length, and thus the length scale of the instability grows. Interestingly, the plot suggests that instability wavelengths will fall within a range between millimeters and a few hundred meters, since the highest flow rates are typically associated with reservoir acidization, where reaction rates are high (red curves).

A reactive-infiltration instability can thus occur in almost any system in which chemical dissolution is coupled with fluid flow. Variations in reaction rate (r), specific reactive area (s), and flow rate (u_0) give rise to a wide range of length scales, from centimeter scale redox fronts in siltstones (Ortoleva, 1994) to kilometer-long scalloping of a dolomitization front (Merino & Canals, 2011). The span of timescales over which the instability develops is also large (Szymczak & Ladd, 2013); acidized plaster (Daccord, 1987) and limestone cores (Hoefner & Fogler, 1988) or salt flushed with water (Kelemen et al., 1995; Golfier et al., 2002) finger in minutes, while geological structures evolve over hundreds of thousands of years. Groundwater velocities are usually small, $u_0 \approx 10^{-8} - 10^{-5}$ cm/s, while the timescale for dissolution, $(rs)^{-1}$, varies from seconds to years; thus both diffusion-dominated ($Drs/u_0^2 \gg 1$) and convection-dominated ($Drs/u_0^2 \ll 1$) dissolution can occur.

The formation of salt sinkholes is an example of diffusion-dominated dissolution; here $rs \approx 2 \times 10^{-4}\,\mathrm{s}^{-1}$ and u_0 is in the range $3 \times 10^{-7} - 3 \times 10^{-6}$ cm/s (Shalev et al., 2006), which means it is in the diffusive (thin-front) regime ($H > 1$). For the large porosity contrast typical of salt dissolution ($\Delta \approx 10$), the maximum unstable wavelength (Fig. 3.16) is then $\lambda_{\max} \approx 0.7 - 7$m, which is in the range of results reported in Shalev et al. (2006). The associated timescales are of the order of $1.5-150$ years (with $\gamma_a \approx 0.18$); thus sinkholes would be expected to develop over tens of years, which is comparable with experimental observations (Shalev et al., 2006).

One important application of reactive-infiltration instability is the formation of wormholes by injecting a low-pH solution into oil or geothermal reservoirs (acidization). This process increases permeability and creates flow paths from the wellbore region to the rock matrix. Wormholes (so named because of their resemblance to channels dug by earthworms) are ramified channels formed due to the dissolution of soluble rock under specific chemical and flow conditions. They are relatively easy to obtain in experiments (Daccord, 1987; Hoefner & Fogler, 1988; Fredd & Fogler, 1998; Golfier et al., 2002; Detwiler et al., 2003; McDuff et al., 2010; Li et al., 2019; Cooper et al., 2023) as illustrated in Fig. 3.17, and have been used for at least 100 years by petroleum engineers to enhance oil and gas production by increasing the permeability of the rock. The shapes of the wormholes formed during acidization depend strongly on the flow rate, with more conical, smoother wormholes forming at lower flow rates, and highly ramified wormholes appearing at high flow rates. Long, thin ("dominant") wormholes, formed at intermediate flow rates, are the most

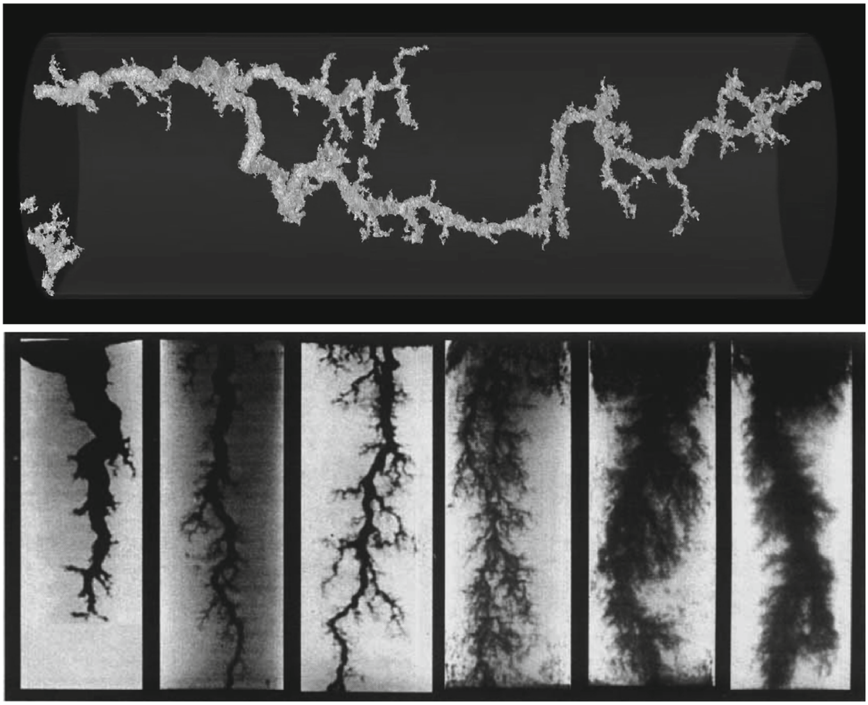

Fig. 3.17 Wormhole formation in porous rocks and fractures. **a**: Tomographic image of a wormhole etched by carbonic acid in limestone core (Cooper et al., 2023). **b**: Neutron radiographs of wormholes formed during the dissolution of limestone by 0.25-M ethylenediaminetetraacetic acid injected at pH 4 (Fredd & Fogler, 1998). The successive panels correspond to volumetric flow rates of $0.01\,\mathrm{cm}^3/\mathrm{min}$, $0.025\,\mathrm{cm}^3/\mathrm{min}$, $0.06\,\mathrm{cm}^3/\mathrm{min}$, $0.15\,\mathrm{cm}^3/\mathrm{min}$, $1\,\mathrm{cm}^3/\mathrm{min}$ and $3\,\mathrm{cm}^3/\mathrm{min}$

effective for petroleum engineering, since they minimize the acid required for a given increase in permeability.

Recently, understanding of wormholing became important when assessing and mitigating the risk of leakage from potential CO_2 sequestration sites, particularly in limestone formations (Ott & Oedai, 2015; Snippe et al., 2020; Luquot & Gouze, 2009; Garcia-Rios et al., 2015; Smith et al., 2013; Hao et al., 2013; Steefel et al., 2013; Elkhoury et al., 2013; Selvadurai et al., 2017; Al-Khulaifi et al, 2019). Carbon dioxide, when mixed with water, becomes aggressive and can dissolve carbonate seams or veins in the caprock, creating CO_2 escape conduits during the sequestration process.

Estimates of wormhole growth rates and, in particular, the so-called breakthrough time (the moment when the longest wormhole reaches the outlet of the system) are crucial for a number of geotechnical problems. These include risk assessment of potential leakage of sequestered carbon dioxide, safety of dam sites in soluble rocks, risk of catastrophic ground subsidence due to solutional widening of fractures, and the danger of water seepage into toxic waste repositories.

Natural wormholes in porous media (except for solution pipes, which we describe in Sect. 3.14) are relatively rare, since large flow rates are needed to trigger the instability, which are not easily obtained under typical pressure gradients in subsurface flows. It is different in the case of rock fractures, where the permeabilities, and thus possible fluid velocities, are much higher. We will return to wormholing in fractures and its link with cave formation in Sect. 3.13.

Fluid velocities during acidization of carbonate reservoirs are larger than in naturally occurring groundwater flows, $u_0 \approx 10^{-3}\,\mathrm{cm/s} - 0.1\,\mathrm{cm/s}$ (Economides & Nolte, 2000), and it is frequently assumed that acidization is convection dominated (Sherwood, 1987; Hoefner & Fogler, 1988). However, rapid dissolution of calcite by concentrated hydrochloric acid (frequently used in acidization), combined with the large reactive surface area of calcite, can lead to reaction rates (rs) as high as $10\,\mathrm{s}^{-1}$ (Cohen et al., 2008), although weaker acids, such has acetic or formic acid, have dissolution rates that are 100 times slower. Thus acidization spans the range from convection-dominated ($H \sim 10^{-4}$) to diffusion-dominated dissolution ($H \sim 100$), but the predicted length scales are always in the sub-centimeter range. At the smallest flow rates ($u_0 \approx 10^{-3}\,\mathrm{cm/s}$), dissolution tends to be diffusion dominated, with a typical length scale of the order of $\lambda_{\max} \approx 0.1\,\mathrm{cm}$, independent of reaction rate. At the highest flow rates ($u_0 \approx 0.1\,\mathrm{cm/s}$) the reactant penetrates downstream, leading to significantly larger scales ($\sim$0.1 cm) than would be predicted from the thin-front limit ($\sim$0.001 cm).

Finally, let us also comment on the stabilization mechanisms of reactive-infiltration instability at shorter wavelengths. In viscous fingering, large k perturbations are stabilized by surface tension. In reactive infiltration, the stabilization mechanism depends on the dissolution regime. In the thin-front limit, $H \gg 1$, as already discussed, the short wavelengths are stabilized by diffusion, and the instability wavelength is comparable to l_u. A somewhat more subtle mechanism is in place in the convective regime ($H \ll 1$). There is now a significant region of partially dissolved material at the dissolution front, which makes the mobility contrast significantly less sharp. The presence of a diffuse interface weakens the instability (Booth, 2008) and leads to the appearance of the maximum growth rate over the length scales comparable to the front thickness, l_d, while keeping $\sigma(k)$ positive as $k \to \infty$ (Szymczak & Ladd, 2011).

3.12 Radial Geometry: Acidized Wells and Ice Stars

> Fain would I stretch me by the highway side,
> To thaw and trickle with the melting snow,

> That mingled soul and body with the tide,
> I too may through the pores of nature flow.
>
> —Henry David Thoreau *The Thaw*

Our results so far have focused on rectangular geometry, where the system dissolves due to the unidirectional flow $u_0\hat{\boldsymbol{e}}_x$ as $x \to \pm\infty$. However, in many natural and engineering systems, the flow is ejected radially outwards from a point source. A key application, discussed earlier, is reservoir acidization. Since acidization is typically carried out using wells, radial geometry represents the most relevant configuration (see Fig. 3.18b).

A strikingly similar process, albeit arising in a completely different context, is the formation of star-like patterns on frozen lakes and rivers (Fig. 3.18a). Whenever a hole forms in the ice cover, relatively warm water (at 4 °C) flows to the surface and melts the snow layer (Knight, 1987; Tsai & Wettlaufer, 2007). This process of snow slush melting by the flowing water can be described by equations analogous to (3.168), but this time tracking the temperature profile instead of the reactant concentration. The positive feedback mechanism remains the same: a small bump on the advancing interface between melted and unmelted regions focuses the flow, leading to increased melting in its vicinity. In the photographs in Figs. 3.1g and 3.18a, the flow lines of the water are beautifully marked on the ice, clearly illustrating the focusing of flow at the tips of the fingers.

The linear stability analysis for the reactive-infiltration instability in the radial case has been detailed in Grodzki and Szymczak (2019). The base solution now corresponds to the radially expanding reaction front

$$R^0(t) = \sqrt{R_0^2 + \frac{\gamma_a}{\varphi_{\max} - \varphi_0}\frac{Q}{\pi}t}, \tag{3.174}$$

where $R_0 = R^0(t = 0)$ and Q is the total fluid flux in the system (in m^2/s). Perturbing the front as

$$\delta R = \varepsilon F(t)\sin(n\varphi), \qquad n \in \mathbf{N}, \tag{3.175}$$

leads to the dispersion relation of the form

$$\tilde{\sigma}(\tilde{n}) \equiv \sigma/\tau = \frac{1}{1+\Gamma}\left[1 - \sqrt{1+4\tilde{n}^2} + \tilde{n}(1-\Gamma)\right] - \frac{1}{\mathrm{Pe}}, \tag{3.176}$$

where the wavenumber, n, is scaled as

$$\tilde{n} = n/\mathrm{Pe}, \tag{3.177}$$

and the Péclet number is defined as

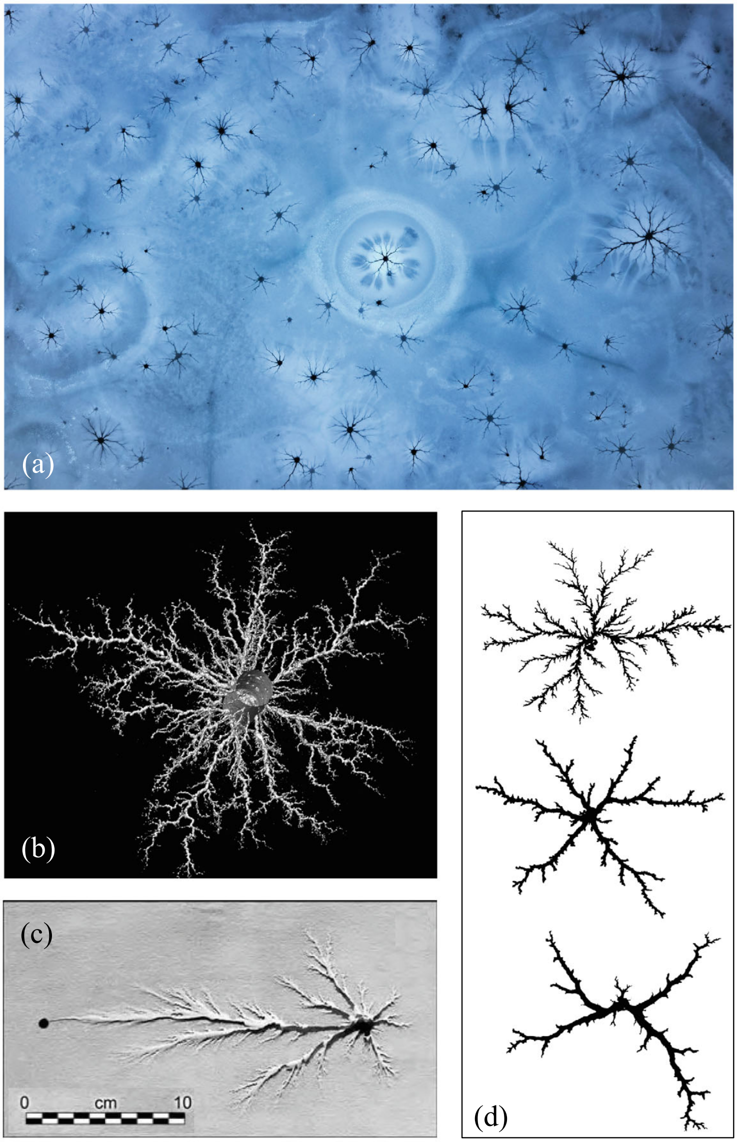

Fig. 3.18 Radial dissolution and melting patterns: **a**: Star-like patterns on a frozen river. **b**: wormholes (30 cm long) formed during carbonate acidization (McDuff et al., 2010), **c** and **d**: Dissolution patterns observed in experiments on the dissolution of blocks of plaster of Paris by Ewers (1982) (**c**) and Daccord (1987) (**d**). The photograph in (**a**) is courtesy of Martin Mecnarowski (www.photomecan.eu). The photo in (**b**) is courtesy of Darren McDuff (ExxonMobil Upstream Research) and the photograph in (**c**) is courtesy of Ralph Ewers

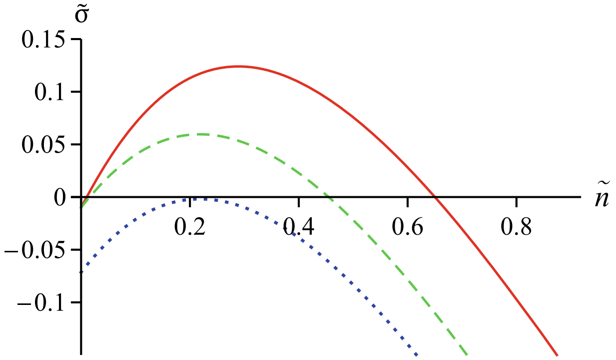

Fig. 3.19 Dispersion relation in radial geometry for $\mathrm{Pe} = 100$, $\Gamma = 0$ (solid line); $\mathrm{Pe} = 100$, $\Gamma = 0.2$ (dashed); $\mathrm{Pe} = 14$, $\Gamma = 0.2$ (dotted)

$$\mathrm{Pe} = \frac{Q}{2\pi D\varphi_{\max}}. \tag{3.178}$$

On the other hand, the growth rate in (3.176) is scaled by the characteristic time over which the front traverses the upstream penetration length

$$\tau = l_u/U_0, \tag{3.179}$$

where $U_0 = \frac{dR^0}{dt}$ is the front velocity, and

$$l_u = \frac{D\varphi_{\max}}{u_0} = \frac{D\varphi_{\max}}{\frac{Q}{2\pi R^0}}. \tag{3.180}$$

The dispersion relations for different values of Pe and Γ are shown in Fig. 3.19. The most unstable mode is given by

$$\tilde{n}_c = \frac{1-\Gamma}{2\sqrt{4-(1-\Gamma)^2}}, \tag{3.181}$$

with the corresponding wavelength

$$\lambda_c = \frac{2\pi R^0}{\tilde{n}_c \mathrm{Pe}} = \frac{4\pi R^0\sqrt{4-(1-\Gamma)^2}}{(1-\Gamma)\mathrm{Pe}}. \tag{3.182}$$

As we see, the most unstable wavelength decreases as the flow rates (and hence Pe) increase. On the other hand, λ_c increases over time as the radial extent of the front, R^0, grows.

The dispersion relation depends on two parameters only: Pe and Γ. Let us now identify the region in the Pe–Γ space where all perturbations are stable, i.e. $\tilde{\sigma}(\tilde{n}_c) \leq 0$.

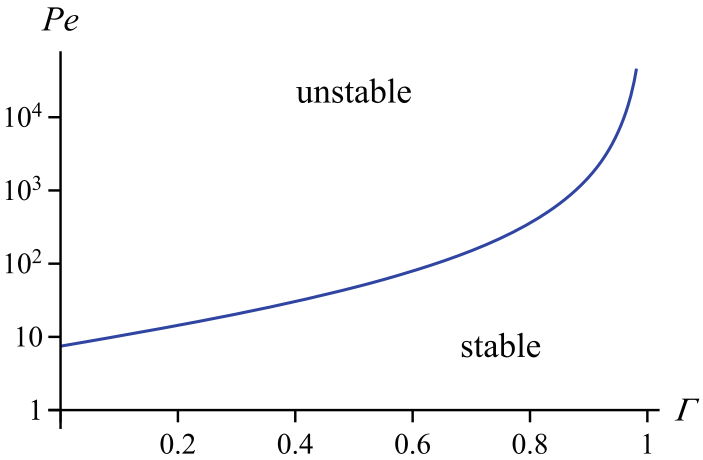

Fig. 3.20 The threshold Péclet number $\mathrm{Pe}_{\mathrm{thr}}$ as a function of the mobility ratio, Γ

For a given Γ, the stable region corresponds to $\mathrm{Pe} < \mathrm{Pe}_{\mathrm{thr}}$, where

$$\mathrm{Pe}_{\mathrm{thr}}(\Gamma) = \frac{2(1+\Gamma)}{2-\sqrt{4-(1-\Gamma)^2}}, \tag{3.183}$$

as shown in Fig. 3.20.

Importantly, Pe (for a given volumetric flow Q) does not depend on the radial extent of the front, R^0. Consequently, we can find the range of Q such that the front will remain stable during its entire evolution.

We note that the dispersion relation for the rectangular geometry, Eq. (3.164), can be obtained from its radial counterpart, Eq. (3.176), in the limit, $R^0 \to \infty$, $u_0 = Q/2\pi R^0 = \text{const.}$ (which implies $Q \to \infty$). In this limit $\tilde{n} \to \tilde{k}$ and $\mathrm{Pe} \to \infty$, and we recover Eq. (3.164).

In fact, this limiting procedure leads to the elimination of the last term (1/Pe) on the rhs of Eq. (3.176). It is this term which shifts the entire dispersion curve downward and results in the appearance of the stable region in the phase diagram of Fig. 3.20. The existence of such an absolute stability region in Fig. 3.20 for the radial dissolution problem is fundamentally different from the behavior of the viscous fingering front in radial geometry, which always becomes unstable at a certain critical radius (Paterson, 1981).

Fig. 3.21 (left) Cemented fractures in shale core (Tang et al., 2021). (right) Fractures and bedding planes in Salzgitter–Salder chalk quarry, Germany (photo by Gretarsson via Wikimedia, distributed under CC BY-SA 4.0 license)

3.13 Cave Formation Paradox

Wind from the sea,
The shimmering candle light,
A drop spread,
The cave of Enoshima.

Akiko Yosano

An important element of our considerations regarding the dissolving fractures is the emergence of the reaction front, which subsequently advances into the fracture. Such a moving front develops once all of the soluble material at the inlet has dissolved. The time needed for such an opening is given by (cf. Eq. (3.110))

$$t_d = \frac{h_{\max} - h_0}{\gamma_a r}. \tag{3.184}$$

Such a setup can serve as an effective model for a range of natural systems, such as fractures in insoluble rock that are partially cemented with a soluble material. Figure 3.21 illustrates one such system: fractures in shales mineralized with calcite. If these fractures reopen, for instance during hydraulic fracturing of shale gas reservoirs, the low-pH fluid can dissolve the cement, creating a setup similar to the Hele–Shaw cell with a soluble bottom.

However, in typical rock fractures or bedding planes (e.g., in the fractured limestone outcrop shown in Fig. 3.21), the entire rock mass is soluble, meaning that $h_{\max}$ is effectively unlimited, and a moving front cannot develop.

Such fractures continue to open, developing exponential profiles of aperture and concentration for linear reaction rates (Fig. 3.22). Indeed, the 1D solutions of Eqs. (3.108)–(3.110) in the limit $h_{\max} \to \infty$ are

$$c_{1D}(x) = c_0 e^{-x/l_d}, \tag{3.185}$$

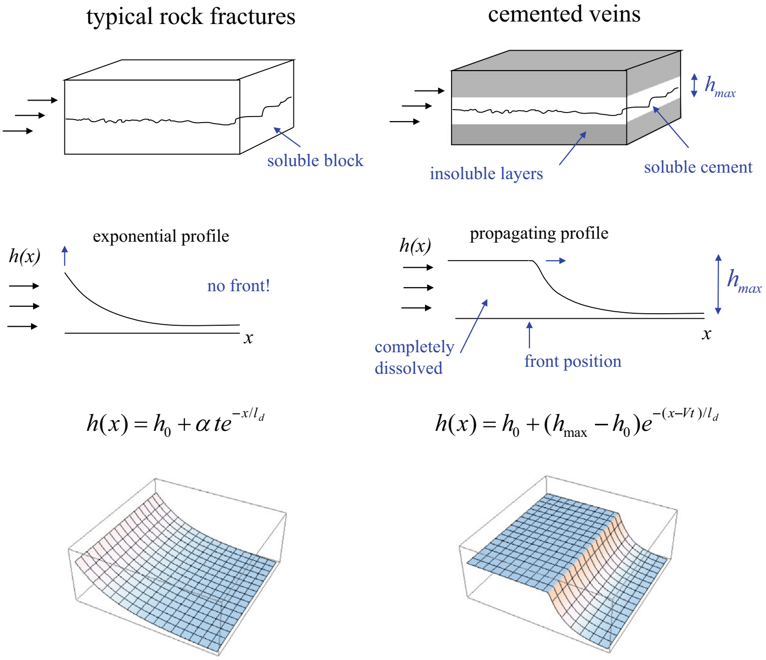

Fig. 3.22 Dissolution of typical rock fractures versus that of cemented veins. In the former case, an exponential concentration profile forms at the inlet with an amplitude that increases over time. In the latter case, the profile propagates into the medium

and

$$h_{1D}(x) = h_0 + 2r\gamma_a t e^{-x/l_d}, \tag{3.186}$$

where, to keep things simple, we neglected diffusion (which corresponds to adopting $H \to 0$ limit). In Eqs. (3.185)–(3.186) the downstream penetration length is given by

$$l_d = \frac{q_0}{2r}. \tag{3.187}$$

There is an extra factor of two compared to Eq. (3.119), because in natural fractures both the upper and lower surface dissolve.

Note that in contrast to Eq. (3.114), the 1D concentration profile is now stationary and does not advance into the fracture. This is a direct consequence of the fact that—unlike in previous considerations—there is no limit to the aperture growth at the inlet. Nevertheless, such a 1D profile can also become unstable (Fig. 3.23), though the physical characteristics of this instability differ from those of the moving-front instability (Szymczak & Ladd, 2011). Interestingly, the limit $H \to 0$ is again fully analytically solvable, although the solutions involve hypergeometric functions (Szym-

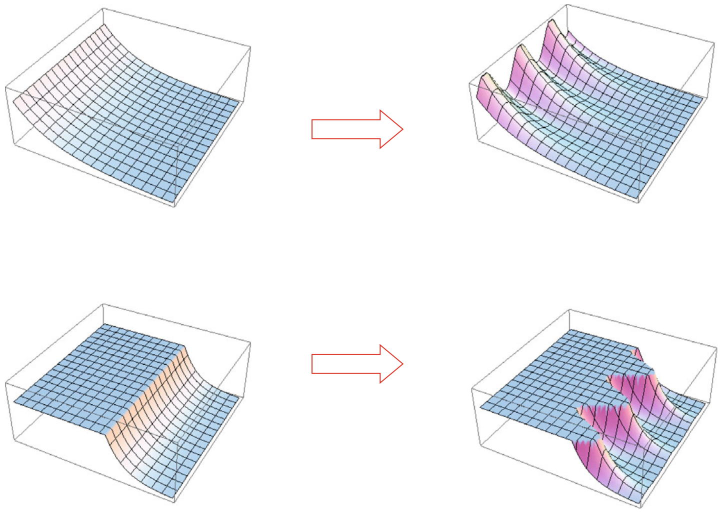

Fig. 3.23 Inlet versus moving front instability: Both profiles shown in Fig. 3.22 are unstable, but these instabilities are characterized by different wavelengths and growth rates

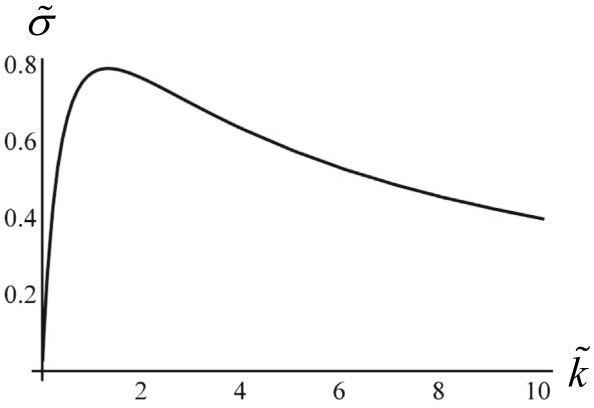

Fig. 3.24 Dispersion relation for the inlet instability in the fractures. The wavenumber is rescaled by the downstream penetration length, $\tilde{k} = l_d k = \frac{q_0}{2r} k$, whereas the growth rate is rescaled by $\tau = \frac{\nu h_0}{2rc_{in}}$, the time it takes for the initial fracture aperture at the inlet to double. For a 0.2 mm fracture dissolved by karst waters, $\tau \approx 5.4 \cdot 10^6$s or 0.17 years (Szymczak & Ladd, 2011)

czak & Ladd, 2011). The maximally unstable wavelength can then be shown to be $\lambda_{\max} = 4.74 l_d = 4.74 \frac{q_0}{2r}$ (see Fig. 3.24).

Let us now try to estimate the characteristic value of l_d for real fractures. The typical values of the parameters characterizing the dissolution of limestone fractures are $r = 2.5 \times 10^{-5}$ cm s^{-1} and $c_0 = 2 \times 10^{-6}$ M cm^{-3} (Dreybrodt, 1996).

Initial fracture apertures range from 0.005 cm to 0.1cm (Motyka & Wilk, 1984; Dreybrodt, 1996; Paillet et al., 1987), and hydraulic gradients are of the order of 10^{-3} to 10^{-1} (Palmer, 1991; Dijk & Berkowitz, 1998). This gives a range of characteristic flow velocities in undissolved fractures from 10^{-4} to 1 cm/s. For these parameter values, the penetration lengths are of the order of centimeters: for example, for $h_0 = 0.02$mm and a hydraulic gradient of 0.01, we find $q_0 = 10^{-3}\,\mathrm{cm}^2\mathrm{s}^{-1}$ and $l_d \approx$ 20 cm. This is exceedingly small when compared to the lengths of karst-incipient fractures and bedding planes (100 m–10 km). Thus, groundwater quickly saturates with calcium ions, and long karst conduits cannot form, at least within the framework of this model. This was noted by White and Longyear (1962), but, interestingly, a similar argument was also raised by Flamache (1896), and was a basis for his dismissal of a dissolution mechanism for cave formation.

One resolution of this paradox was proposed by White (1977), who, based on experimental data on calcite dissolution (Plummer & Wigley, 1976), suggested that the formation of large cave systems could be explained by the sharp decline in the dissolution rate of $CaCO_3$ near saturation. This is commonly referred to as the "kinetic trigger" mechanism in the speleogenesis literature. The kinetic trigger mechanism can be modeled as a transition from linear to higher-order kinetics at a threshold concentration

$$R(c) = \begin{cases} r(c_{\mathrm{sat}} - c), & c < c_{\mathrm{th}} \\ r_n(c_{\mathrm{sat}} - c)^n, & c > c_{\mathrm{th}}. \end{cases} \tag{3.188}$$

The nonlinear reaction law then leads to a power-law concentration profile

$$c_{\mathrm{sat}} - c \sim x^{\frac{1}{1-n}} \tag{3.189}$$

rather than the exponential profile given by Eq. (3.185). This results in increased penetration lengths and facilitates fracture opening over the geologically reasonable timescales, at least in the case of fractures with relatively large initial apertures (Dreybrodt, 1990, 1996).

However, it seems that there is a simpler resolution to the cave-formation paradox, not based on the subtleties of chemical kinetics. As we already know, fractures do not dissolve uniformly; instead, the dissolution front evolves into fingers. While cave formation initially occurs along fractures and bedding planes, which have planar, slot-like geometries, the mature cave system is almost always a network of pipe-like conduits, as shown in Fig. 3.25. This suggests that fracture dissolution is inherently a 2D process, making a 1D model unsuitable in this context (Szymczak & Ladd, 2011).

In the later stages of dissolution, the undulations of the front evolve into well-defined finger-like channels that rapidly advance into the fracture, leading to its opening at much earlier times than in the homogeneous (one-dimensional) case. As dissolution progresses, the fingers interact, competing for the available flow, and eventually the shorter ones stop growing (see Fig. 3.26).

The mechanism of competition is further elucidated in Fig. 3.27. As observed, there are many more fingers visible in the aperture map (center) than in either the concentration (left) or flow map (right). In fact, the channels compete for flow, with the longer ones capturing a larger portion of it due to higher pressure gradients at their tips. Larger flows and greater penetration lengths in longer channels lead to their faster growth compared to shorter ones, which, deprived of flow, quickly become saturated and cease growing, thus losing the competition. On the other hand, the longer channels again compete for the flow between themselves, which leads to the emergence of a hierarchical structure, with many short channels, and only a few long ones. This is essentially the same positive feedback loop between flow, transport, and reaction that led to the formation of the channel in the first place, but now acting in a nonlinear regime. As a result, the characteristic distance between the active channels, d, steadily increases. The fluid flux within the active channels, q^{chann}, increases as well, approximately in proportion to d/w:

$$q^{\text{chann}} = q_0 d/w, \tag{3.190}$$

where q_0 is the average initial fluid flux in the fracture and w is the width of the channels (Fig. 3.28).

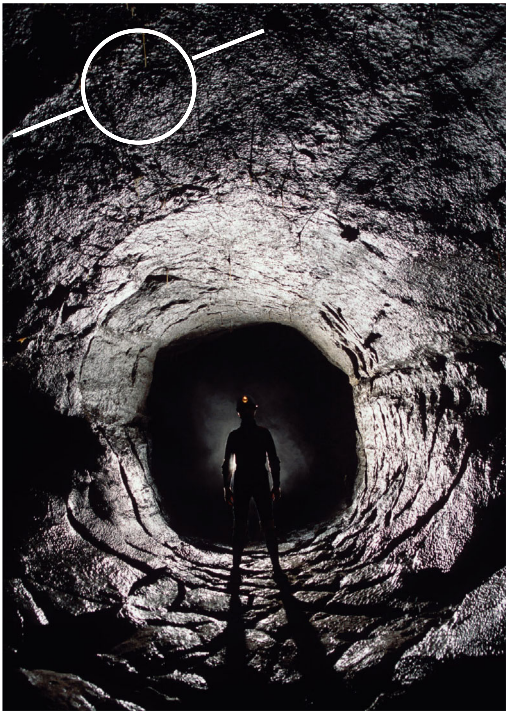

Fig. 3.25 The conduit in a phreatic cave in Dan Yr Ogof, Swansea Valley, South Wales (photo courtesy of Brendan Marris, Dudley Caving Club) and a schematic cross section of the conduit, showing the initial fissure (inset)

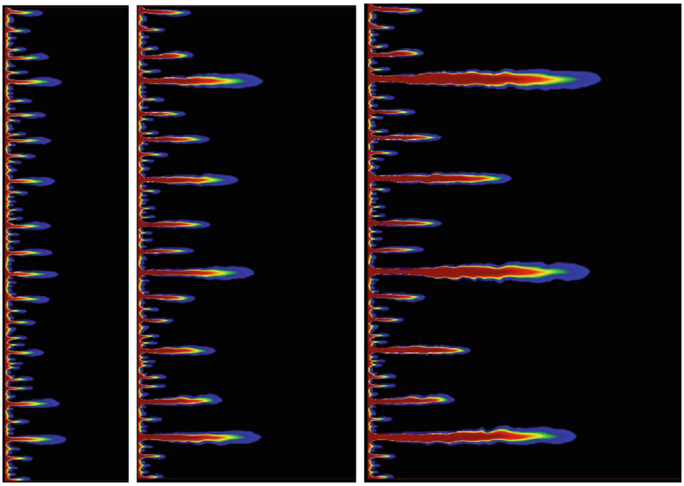

Fig. 3.26 Evolution of the aperture field over time from numerical simulations of the dissolution of a single fracture. Competition between the channels results in the emergence of a hierarchical pattern, characterized by many short channels and a few long ones. The red shading represents the deepest erosion, while dark gray/blue correspond to the least erosion; the intermediate colors are yellow (higher) and green (lower)

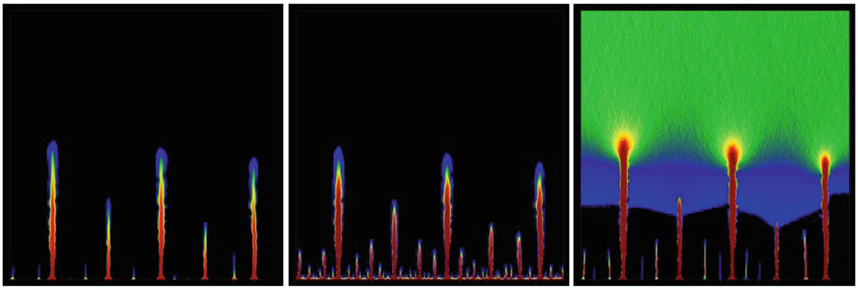

Fig. 3.27 Concentration (left), aperture (center) and flow profiles (right) in a dissolving fracture. Red shading represents regions of highest undersaturation/aperture/flow magnitude, followed by green, blue, and black

Eventually, d reaches the scale of the fracture width, leaving only one active channel left in the system. At this moment, the penetration length in the channel approaches

$$l_d^{\text{chann}} = \frac{q_0 W}{2rw}, \tag{3.191}$$

which is usually several orders of magnitude larger than the initial penetration length given by Eq. (3.187). Thus the flow focusing in the channels provides an alternative

Fig. 3.28 Flow focusing in the dissolution channels: the channel of width w attracts the flow from the region of a linear extent d (equal to the characteristic distance between the channels)

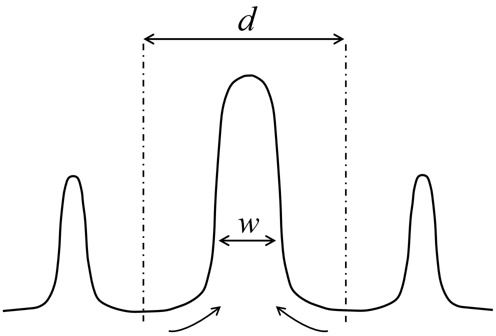

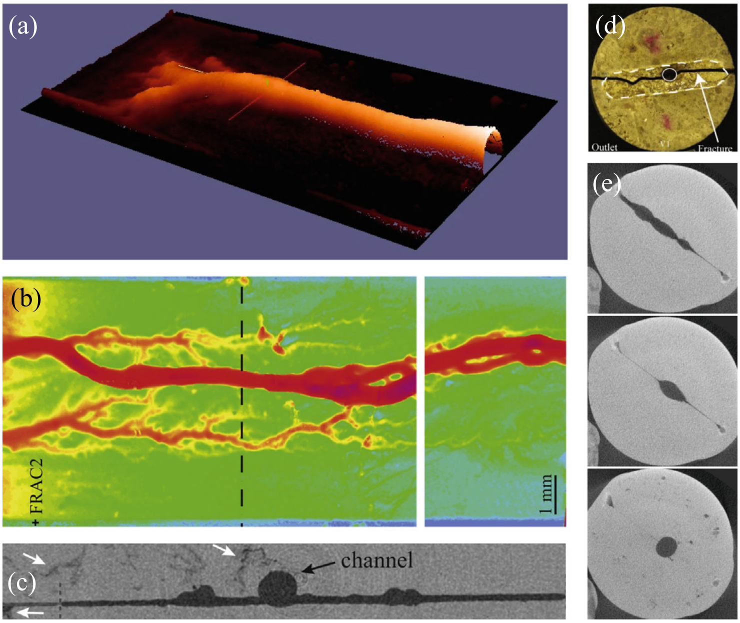

Fig. 3.29 **a** and **e**–wormhole formation during the dissolution of limestone fractures by CO_2-rich solution (Garcia-Rios et al., 2015). Microtomographic image (**a**) and microscopic images of cross-sections (**e**). **b** and **c**—Wormholes formed during the dissolution of limestone fractures by HCl solution (Noiriel & Deng, 2018): aperture map based on the microtomographic data (**b**) and microscopic image of the cross-section (**c**). **d**—Conduit formation during limestone fracture dissolution by CO_2-rich brine (Elkhoury et al., 2013). The photos in a and e are courtesy of Linda Luquot, University of Montpellier

mechanism for the increase of penetration length and hence for the possibility of karst conduit formation, even in the absence of a kinetic trigger.

Instabilities in fracture dissolution were first discovered through numerical simulations (Hanna & Rajaram, 1998) and later confirmed by experiments (Detwiler et al., 2003; Gouze et al., 2003; Elkhoury et al., 2013; Garcia-Rios et al., 2015; Osselin et al., 2016; Noiriel & Deng, 2018), as presented in Fig. 3.29. The experiments elegantly demonstrate the transition from fracture flow to conduit flow, with the conduits assuming a regular, circular form (Fig. 3.29c–e), resembling phreatic cave passages (Fig. 3.25).

Returning to the cemented fractures of Fig. 3.21, one can ask whether instabilities are important in their dissolution dynamics. In nature, reactive-infiltration instability in such fractures is rarely observed since the cementation prevents appreciable flow in such systems. However, in engineering applications, these fractures can be reactivated using methods such as hydraulic fracturing, often used e.g. in the stimulation of shale reservoirs. Alas, the presence of carbonate lamina within the fractures can impede methane transport from the matrix to the fractures. A potential remediation strategy is to acidize the reopened fractures by treating them with a low-pH solution (Szymczak et al., 2019), aiming to induce dissolutional instabilities. This approach offers two main advantages: On the one hand, dissolution helps in removing the carbonate lamina, which hinders fracture/matrix transfer. On the other hand, inhomogeneous dissolution patterns help sustain fluid flow, preventing the resealing of the fracture as fluid pressure is removed. This occurs because the less-dissolved regions act as supports, keeping the more dissolved regions open.

The final question we would like to address, in the context of the initial and moving front instabilities depicted in Fig. 3.23, is which of these two instabilities would be observed in a fracture with an initial aperture h_0 and a maximum aperture $h_{\max}$? To answer this, it is necessary to compare the characteristic development time of the initial instability, associated with the exponential profile, to the fracture opening time t_d (3.184). This comparison is mainly governed by the parameter $\Delta_h = \frac{(h_{\max} - h_0)}{h_0}$, which represents the ratio of the depth of the soluble layer to the initial aperture of the fracture (Szymczak & Ladd, 2011) and is defined analogously to the porosity contrast (3.173). For thick soluble layers, where $\Delta_h \gg 1$, the initial instability will be significant. Conversely, for $\Delta_h < 1$, the moving front will develop first, eventually breaking into fingers.

A detailed experimental study of the initial instability in Hele–Shaw cells with a soluble bottom was performed by Osselin et al. (2016). The reaction front was extracted from photographic images at the early stages of dissolution and analyzed using the Fourier transform to decompose the signal into sinusoidal modes, as illustrated in Fig. 3.30, The position of the maximum of the spectrum corresponds to the fastest-growing mode, the wavelength of which was then compared with theoretical predictions, showing quite good agreement (to within a few percent).

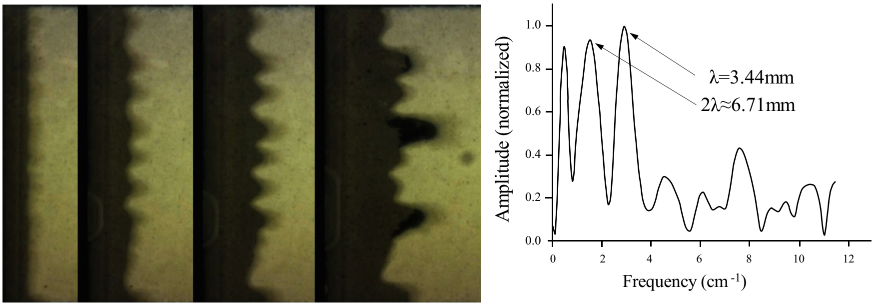

Fig. 3.30 (left) Advancement of the dissolution front and the onset of the instability in a Hele–Shaw cell with a soluble bottom (Fig. 3.9), with an initial aperture of $h_0 = 100\,\mu\text{m}$, a maximum aperture of $h_{\max} = 600\,\mu\text{m}$ and a flow rate of 0.25mL/hr. The successive photographs correspond to 4.3, 6.2, 8.3 and 10.8 days (Osselin et al., 2016). (right) Spectral analysis of the dissolution front for this experiment (after 2.4 days). The position of the main peak (3.44 mm) compares well with the theoretical predictions (3.50 mm)

3.14 Solution Pipes

> The whole ground is one huge hole. Holes are the only features of the landscape: big holes, little holes, damp ones, smelly ones; holes occupied and holes to let; holes you fall into and holes you don't—but, holes. Everywhere holes.
>
> Sapper—*No Man's Land*

Intriguing natural examples of dissolution fingers are solution pipes (Fig. 3.31)—vertical, finger-like structures found in the epikarst zone of porous calcareous rocks. They vary in size, ranging from a few centimeters to several meters in diameter, but are typically less than 1 m wide, with variable depths, the deepest reaching 100 m. They also vary in shape: some are conical, tapering gradually toward the tip, while others are strongly elongated, maintaining an almost constant cross-section with a cigar-shaped termination. Their cross-sections are almost perfectly circular and remarkably smooth (Fig. 3.31e–h), creating the impression that they were artificially drilled rather than naturally formed.

One of the first to describe the morphology of solution pipes in detail was Charles Lyell, the father of modern geology. His 1839 paper "On the tubular cavities filled with gravel and sand called sand-pipes in the chalk near Norwich" (Lyell, 1839) remains a remarkable example of deductive reasoning based on natural observations. Lyell describes a group of solution pipes in chalk strata (see Fig. 3.32), noting their elongated shape (reaching lengths of up to 20 m) and circular cross-sections. He also comments that these pipes do not merge, tend to stay separated from one another, and are not guided by the fractures.

Fig. 3.31 Solution pipes: **a**—pipes in Cretaceous chalk (Swanscombe, UK); **b**—pipes in Quaternary calcarenite (Cape Bridgewater, Australia), **c**, **e**–**g**—pipes in Miocene calcarenite, (Smerdyna quarry, Poland); **d**—pipes in Neogene calcarenite (Guilderton quarry, Australia); **h**—pipe in Pleistocene calcarenite at Cape Perron, Perth, Australia. Photo in (**a**) is by J. Rhodes, courtesy of British Geological Survey. Source: BGS GeoScenic (image P201858)

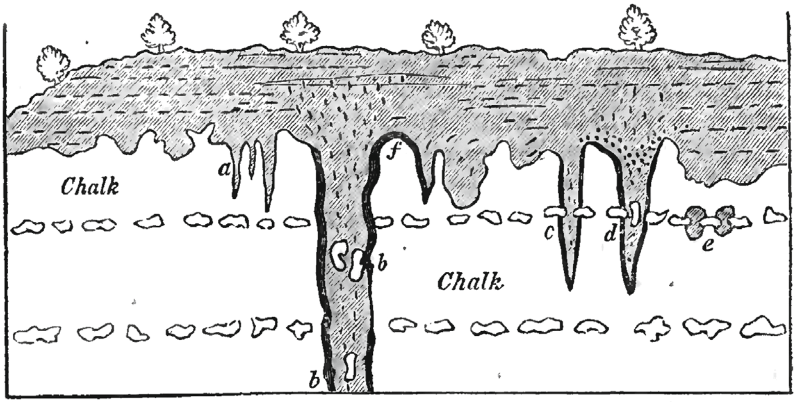

Fig. 3.32 Solution pipes in the chalk at Eaton, near Norwich, as sketched by Charles Lyell (Lyell, 1839)

When smaller pipes intersect horizontal layers of flint nodules (c & d in the figure), the nodules tend to remain in place, sticking out of the pipe. In contrast, in larger pipes (b), the nodules are displaced slightly downward from their original positions. These observations led Lyell to the hypothesis that the pipes are of solutional origin, with the chalk having been removed by the corroding action of water charged with acid. The flint nodules, being insoluble, were left in situ in the smaller pipes after the calcareous matrix had dissolved. He also concludes, from the manner in which the large detached flints were dispersed through the contents of the widest pipes, that the excavation and filling of the pipe were gradual and contemporaneous processes. He further comments that the fact that piping always occurs under the cover of sand or gravel, and never on the exposed rock, may be related to the way these upper layers provide space for the water to focus.

Not all researchers agreed with Lyell. In particular, Trimmer (1845) expressed the opinion that the pipes originated from the mechanical action of water, similar to potholes near waterfalls. However, as argued by Prestwich (1855), this would imply that they were empty during their formation, meaning that all the insoluble material (such as the flint nodules in Fig. 3.32) should be found at the bottom of the pipes, which is not the case. Additionally, the pipes do not appear to contain grinding tools required for pothole erosion (e.g., resistant pebbles), Furthermore, some of the pipes have an enormous aspect ratio (even 100:1), much larger than any known potholes, making it difficult to imagine that the vortices of such an elongation could actively carve out pipes.

The pipes in tropical and Mediterranean climates differ from those in temperate regions, as they often feature hard rims cemented with calcite (see Fig. 3.31b). In some areas, the eroded matrix around the pipes reveals a reversed landscape, resembling a forest of vertical pipes standing closely together. The resemblance of these pipes to tree trunks has historically led to their misidentification as petrified trees (Bretz, 1960;

Boutakoff, 1963). This model suggested that decaying tree trunks, rapidly buried by aeolian sand, could form conduits for groundwater, leading to the precipitation of calcrete and the formation of a solid cast around the original trunk.

However, this hypothesis was challenged by several researchers (Herwitz, 1993; Grimes, 2004), who noted that the close spacing of the pipes (less than 0.5 m in some places) is too dense for a forest, the bases of the pipes are rounded hemispheres without paleosol horizons or branching root structures (Grimes, 2004), and some pipes reach depths of up to 20 m and are unbranched vertical cylinders, which would imply rather peculiar, column-like trees. Despite these objections, interpretive signs erected at Cape Bridgewater (Fig. 3.31b) in the early 2000s still described these structures as a petrified forest (Grimes, 2004).

It seems that the only hypothesis that has withstood scrutiny posits that the rimmed pipes in tropical climates are solutional in origin (Lundberg & Taggart, 1995; De Waele et al., 2011; Lipar et al., 2015, 2021), i.e., their genesis is similar to that postulated by Lyell for the chalk pipes in England, with the only difference being the rim cementation triggered by high evaporation rates in tropical climates. The formation of the pipes would then be linked to the reactive-infiltration instability—small inhomogeneities in the porous matrix tend to focus the flow, which is followed by enhanced dissolution, which eventually transforms the initial inhomogeneities into mature pipes.

A question remains regarding the sources of the large masses of water that carved the pipes. While most researchers suggest that it is CO_2-charged rainwater acting over millennia, an alternative hypothesis exists for pipes formed in colder areas, which links their formation to deglaciation. Morawiecka and Walsh Morawiecka & Walsh (1997), Walsh and Morawiecka-Zacharz Walsh & Morawiecka-Zacharz (2001) and Dobrowolski and Mroczek Dobrowolski & Mroczek (2015) studied pipes in Poland that could have formed subglacially under the cover of a continental glacier till. Piping there is restricted to areas beneath a till cover, and pipes did not develop where till is absent. This links the formation of the pipes to the deglaciation at the end of the Elsterian period, when large volumes of cold water were suddenly released into the fully saturated subglacial aquifer. In such conditions, karstification becomes very intense (Lauritzen & Skoglund, 2013).

While solution pipes and wormholes are associated with the dissolution of the rock, replacement fingers are linked to dissolution-precipitation processes, where the primary mineral is replaced by a secondary one (Korzhinskii, 1968; Putnis, 2009; Kondratiuk et al., 2017). Examples include dolomitization (Fig. 3.33a), where limestone (calcium carbonate) is replaced by dolomite (calcium magnesium carbonate). Since the molar volume of dolomite is smaller than that of calcite, the primary mineral in limestone, dolomitization can create additional pore space if it is not accompanied by significant compaction or cementation. The increased permeability of the dolomite can then trigger instability, which can lead to the formation of dolomite fingers (Koeshidayatullah et al., 2020; Centrella et al., 2021; Merino & Canals, 2011). Another example is the formation of uranium rolls (Fig. 3.33b), where uraninite precipitates at the redox front that separates oxidized rock from reduced rock. The oxidized rock becomes more porous than the reduced rock because redox reactions

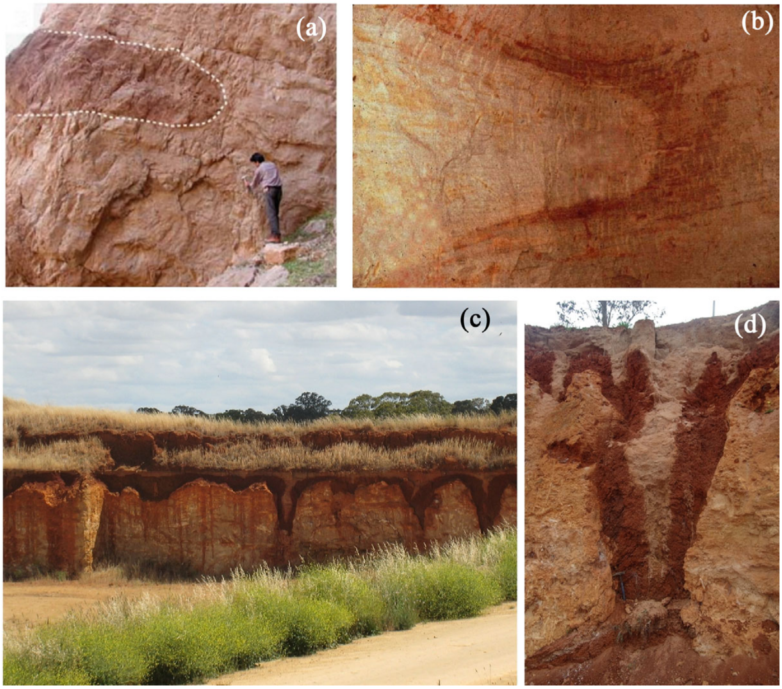

Fig. 3.33 **a**: A dolomite finger in limestone (Sharp et al., 20110) **b**: Uranium roll with uraninite precipitation around its tip. The photo is by C. L. Van Alstine of the U. S. Atomic Energy Commission (courtesy of dr Robert Gregory, Wyoming State Geological Survey) **c**: Terra rossa fingers at Greatstone Winery near Coonawarra, South Australia. The photo is courtesy of Les Sampson (Claremont Wines, South Australia). **d**: Closeup of one of the fingers, showing the terra rossa layer (dark red) and more recent siliceous sands overlaying it

produce sulfuric acid that dissolves potassium feldspars. Increased porosity again results in instability leading to the formation of characteristic fingers with a thin band (Dewynne et al., 1993) of uraninite. Finally, Fig. 3.33c and d show terra-rossa fingers above limestone. An intriguing hypothesis for their genesis has been put forward by Merino and Banerjee (2008), suggesting that terra-rossa forms through the authigenic replacement of the underlying limestone at a reaction front. The hydrogen ions produced in such a reaction further dissolve the rock matrix, triggering a reactive-infiltration instability which could result in intense piping (Kondratiuk et al., 2017).

3.15 Coda

> “Begin at the beginning,” the King said, very gravely,

> "and go on till you come to the end: then stop".
>
> —Lewis Carrol *Alice's Adventures in Wonderland*

This necessarily brief overview of viscous and reactive instabilities was not intended to serve as a comprehensive review of all structures, patterns, flow, and reaction regimes. Instead, it aimed to highlight the fundamental physical mechanisms behind the formation of these forms, as well as to draw the reader's attention to their beauty and encourage independent observation of their occurrence in nature.

Let us conclude by raising some open questions regarding the relationship between the shapes of viscous fingers and dissolution fingers in the nonlinear regime. A striking observation when comparing the shape of solution pipes (Fig. 3.31) and wormholes (Fig. 3.17) is the relative smoothness of the former. Looking back at the asymptotic forms of the viscous fingers (Fig. 3.8), one cannot help but notice that wormholes share similarities with viscous fingers in porous media (Fig. 3.8b). In contrast, solution pipes, with their smoothness and geometric regularity, resemble the Saffman–Taylor finger (Fig. 3.8a). Could solution pipes, then, be the asymptotic, time-invariant solutions of the dissolution equations? If so, might it be possible to derive such an asymptotic shape and prove its time-invariance?

Wait a moment!—someone might say. The Saffman–Taylor finger appears in experiments conducted in a noise-free system (empty Hele–Shaw cell), while both solution pipes and wormholes develop in highly disordered porous media. Why, then, is one smooth and the other fractal? We would like to leave readers with this questions (and others) highlighting that we are far from a complete understanding of these systems.

Acknowledgements I would like to thank my collaborators, without whom the results presented here would never have been obtained, especially Tony Ladd, with whom I have jointly studied reactive-infiltration instability for the last 20 years, as well as Einat Aharonov, Agnieszka Budek, Max P. Cooper, Michał Dzikowski, Filip Dutka, Piotr Grodzki, Kamil Kwiatkowski, Paweł Kondratiuk, Silvana Magni, Florian Osselin, Michał Pecelerowicz, Andrzej Radliński, Roi Roded, Rishabh Prakash Sharma, Tomasz Szawełło, Virat Upadhyay, Hanna Trędak, Dawid Woś and Stanisław Żukowski. Inspiring discussions with the late H. Scott Fogler are also gratefully acknowledged.

References

Acheson, D. J. (1990). *Elementary fluid dynamics*. Oxford University Press.

Al-Khulaifi, Y., Lin, Q., Blunt, M. J., & Bijeljic, B. (2019). Pore-scale dissolution by CO_2 saturated brine in a multimineral carbonate at reservoir conditions: Impact of physical and chemical heterogeneity. *Water Resources Research, 55*, 3171–3193.

Balakotaiah, V. (2004). Hyperbolic averaged models for describing dispersion effects in chromatographs and reactors. *Korean Journal of Chemical Engineering, 21*(3A), 318–328.

Bear, J. (1972). *Dynamics of fluids in porous media*. Dover.

Ben-Jacob, E., Shmueli, H., Shochet, O., & Tenenbaum, A. (1992). Adaptive self-organization during growth of bacterial colonies. *Physica A, 187*, 378–424.

Ben-Jacob, E., Cohen, I., & Gutnick, D. (1998). Cooperative organization of bacterial colonies: From genotype to morphotype. *Annual Review of Microbiology, 52*, 779–806.

Booth, R. (2008). *Miscible flow through porous media*. Ph.D. thesis, University of Oxford.

Boutakoff, N. (1963). The geology and geomorphology of the Portland area. *Geological Survey of Victoria Memoir, 22*, 1–172.

Bretz, J. H. (1960). Bermuda: A partially drowned, late mature, Pleistocene karst. *Geological Society of America Bulletin, 71*, 1729–1754.

Centrella, S., Beaudoin, N. E., Derluyn, H., Motte, G., Hoareau, G., Lanari, P., Piccoli, F., Pecheyran, C., & Callot, J. P. (2021). Micro-scale chemical and physical patterns in an interface of hydrothermal dolomitization reveals the governing transport mechanisms in nature: Case of the Layens anticline, Pyrenees, France. *Sedimentology, 68*, 834–854.

Chadam, D., Hoff, D., Merino, E., Ortoleva, P., & Sen, A. (1986). Reactive infiltration instabilities. *Journal of Applied Mathematics, 36*, 207–221.

Cohen, C., Ding, D., Quintard, M., & Bazin, B. (2008). From pore scale to wellbore scale: Impact of geometry on wormhole growth in carbonate acidization. *Chemical Engineering Science, 63*, 3088–3099.

Colombani, J. (2008). Measurement of the pure dissolution rate constant of a mineral in water. *Geochimica et Cosmochimica Acta, 72*, 5634–5640.

Cooper, M. P., Sharma, R. P., Magni, S., Blach, T. P., Radlinski, A. P., Drabik, K., Tengattini, A., & Szymczak, P. (2023). 4D tomography reveals a complex relationship between wormhole advancement and permeability variation in dissolving rocks. *Advances in Water Resources, 175*, Article 104407.

Couder, Y. (2000). Viscous fingering as an archetype for growth patterns. In G. Batchelor, H. Moffatt, & M. Worster (eds.), *Perspectives in Fluid Dynamics* (pp. 53–104). Cambridge University Press Cambridge.

Couder, Y., Argoul, F., Arnéodo, A., Maurer, J., & Rabaud, M. (1990). Statistical properties of fractal dendrites and anisotropic diffusion-limited aggregates. *Physical Review A, 42*, 3499–3503.

Couder, Y., Maurer, J., González-Cinca, R., & Hernández-Machado, A. (2005). Side-branch growth in two-dimensional dendrites. I. Experiments. *Physical Review E, 71*(3), 31602.

Daccord, G. (1987). Chemical dissolution of a porous medium by a reactive fluid. *Physical Review Letters, 58*(5), 479–482.

De Waele, J., Lauritzen, S.-E., & Parise, M. (2011). On the formation of dissolution pipes in Quaternary coastal calcareous arenites in Mediterranean settings. *Earth Surface Processes and Landforms, 36*(2), 143–157.

Detwiler, R. L., Glass, R. J., & Bourcier, W. L. (2003). Experimental observations of fracture dissolution: The role of Péclet number in evolving aperture variability. *Geophysical Research Letters, 30*, 1648.

Dewynne, J. N., Fowler, A. C., & Hagan, P. S. (1993). Multiple reaction fronts in the oxidation/reduction of iron-rich uranium ores. *SIAM Journal on Applied Mathematics, 53*, 971–989.

Dijk, P., & Berkowitz, B. (1998). Precipitation and dissolution of reactive solutes in fractures. *Water Resources Research, 34*, 457–470.

Dobrowolski, R., & Mroczek, P. (2015). Clay cortex in epikarst forms as an indicator of age and morphogenesis-case studies from Lublin-Volhynia chalkland (East Poland, West Ukraine). *Geomorphology, 247*, 66–75.

Dreybrodt, W. (1990). The role of dissolution kinetics in the development of karst aquifers in limestone: A model simulation of karst evolution. *The Journal of Geology, 98*, 639–655.

Dreybrodt, W. (1996). Principles of early development of karst conduits under natural and man-made conditions revealed by mathematical analysis of numerical models. *Water Resources Research, 32*, 2923–2935.

Economides, M. J., & Nolte, K. G. (2000). *Reservoir stimulation*. Wiley.

Elkhoury, J. E., Ameli, P., & Detwiler, R. L. (2013). Dissolution and deformation in fractured carbonates caused by flow of CO_2-rich brine under reservoir conditions. *International Journal of Greenhouse Gas Control, 16*, S203–S215.

Ewers, R. O. (1982). *Cavern development in the dimensions of length and breadth*. Ph.D. thesis, McMaster University.

Flamache, A. (1896). Sur la formation des grottes et des vallees souterraines. *Société Belge Géologie Paléontologie et d'Hydrologie, 9*, 355–367.

Fredd, C. N., & Fogler, H. S. (1998). Influence of transport and reaction on wormhole formation in porous media. *AIChE Journal, 44*, 1933–1949.

Garcia-Rios, M., Luquot, L., Soler, J. M., & Cama, J. (2015). Influence of the flow rate on dissolution and precipitation features during percolation of CO_2-rich sulfate solutions through fractured limestone samples. *Chemical Geology, 414*, 95–108.

Golding, I., Kozlovsky, Y., Cohen, I., & Ben-Jacob, E. (1998). Studies of bacterial branching growth using reaction-diffusion models for colonial development. *Physica A, 260*, 510–554.

Golfier, F., Zarcone, C., Bazin, B., Lenormand, R., Lasseux, D., & Quintard, M. (2002). On the ability of a Darcy-scale model to capture wormhole formation during the dissolution of a porous medium. *Journal of Fluid Mechanics, 457*, 213–254.

Gouze, P., Noiriel, C., Bruderer, C., & Loggia, D. (2003). X-ray tomography characterization of fracture surfaces during dissolution. *Geophysical Research Letters, 30*, 1267.

Grimes, K. G. (2004). Solution Pipes or Petrified Forests? Drifting sands and drifting opinions! *The Victorian Naturalist, 121*(1), 14–22.

Grodzki, P., & Szymczak, P. (2019). Reactive-infiltration instability in radial geometry: From dissolution fingers to star patterns. *Physical Review E, 100*, Article 033108.

Gustafsson, B., Teodorescu, R., & Vasil'ev, A. (2014). *Classical and stochastic Laplacian growth*. Springer.

Hanna, R. B., & Rajaram, H. (1998). Influence of aperture variability on dissolutional growth of fissures in karst formations. *Water Resources Research, 34*, 2843–2853.

Hao, Y., Smith, M., Sholokhova, Y., & Carroll, S. (2013). CO_2-induced dissolution of low permeability carbonates. Part II: Numerical modeling of experiments. *Advances in Water Resources, 62*, 388–408.

Herwitz, S. R. (1993). Stemflow influences on the formation of solution pipes in Bermuda eolianite. *Geomorphology, 6*(3), 253–271.

Hill, S. (1952). Channeling in packed columns. *Chemical Engineering Science, 1*, 247–253.

Hoefner, M. L., & Fogler, H. S. (1988). Pore evolution and channel formation during flow and reaction in porous media. *AIChE Journal, 34*, 45–54.

Homsy, G. M. (1987). Viscous fingering in porous media. *Annual Review of Fluid Mechanics, 19*, 271–311.

Howison, S. D. (2000). A note on the two-phase Hele-Shaw problem. *Journal of Fluid Mechanics, 409*, 243–249.

Kelemen, P., Whitehead, J., Aharonov, E., & Jordahl, K. (1995). Experiments on flow focusing in soluble porous media, with applications to melt extraction from the mantle. *Journal of Geophysical Research, 100*, 475–496.

Knight, C. A. (1987). Slush on lakes. In Loper, D. E. (Eds.), *Structure and dynamics of partially solidified systems* (pp. 453–465). Martinus Nijhoff.

Koeshidayatullah, A., Corlett, H., Stacey, J., Swart, P. K., Boyce, A., & Hollis, C. (2020). Origin and evolution of fault-controlled hydrothermal dolomitization fronts: A new insight. *Earth and Planetary Science Letters, 541*, Article 116291.

Kondratiuk, P., & Szymczak, P. (2015). Steadily translating parabolic dissolution fingers. *SIAM Journal of Applied Mathematics, 75*, 2193–2213.

Kondratiuk, P., Tredak, H., Upadhyay, V., Ladd, A. J. C., & Szymczak, P. (2017). Instabilities and finger formation in replacement fronts driven by an oversaturated solution. *Journal of Geophysical Research: Solid Earth, 122*, 5972–5991.

Korzhinskii, D. S. (1968). The theory of metasomatic zoning. *Mineralium Deposita, 231*, 222–231.

Kuhn, A., & Argoul, F. (1994). Spatiotemporal morphological transitions in thin-layer electrodeposition: The Hecker effect. *Physical Review E, 49*(5), 4298–4305.

Ladd, A. J. C., & Szymczak, P. (2017). Use and misuse of large-density asymptotics in the reaction-infiltration instability. *Water Resources Research, 53*(3), 2419–2430.

Lauritzen, S. E., & Skoglund, R. Ø. (2013). Glacier ice-contact speleogenesis in marble stripe karst. In *Proceedings of the 16th International Congress of Speleology, July 21–28, Brno* (Vol. 3, pp. 363–396). Academic, San Diego.

Li, W., Einstein, H. H., & Germaine, J. T. (2019). An experimental study of matrix dissolution and wormhole formation using gypsum core flood tests: 1. Permeability evolution and wormhole geometry analysis. *Journal of Geophysical Research: Solid Earth, 124*, 11055–11073.

Lipar, M., Webb, J. A., White, S. Q., & Grimes, K. G. (2015). The genesis of solution pipes: Evidence from the Middle-Late Pleistocene Bridgewater Formation calcarenite, southeastern Australia. *Geomorphology, 246*, 90–103.

Lipar, M., Szymczak, P., White, S. Q., & Webb, J. A. (2021). Solution pipes and focused vertical water flow: Geomorphology and modelling. *Earth-Science Reviews, 218*, Article 103635.

Løvoll, G., Méheust, Y., Toussaint, R., Schmittbuhl, J., & Måløy, K. J. (2004). Growth activity during fingering in a porous Hele-Shaw cell. *Physical Review E, 70*, Article 026301.

Lundberg, J., & Taggart, B. E. (1995). Dissolution pipes in northern Puerto Rico: An exhumed paleokarst. *Carbonates Evaporites, 10*(2), 171–183.

Luquot, L., & Gouze, P. (2009). Experimental determination of porosity and permeability changes induced by injection of CO_2 into carbonate rocks. *Chemical Geology, 265*(1–2), 148–159.

Lyell, C. (1839). On the tubular cavities filled with gravel and sand called "Sand-pipes", in the chalk near Norwich. *Philosophical Magazine, 15*(96), 257–266.

McDuff, D. R., Shuchart, C. E., Jackson, S. K., Postl, D., & Brown, J. S. (2010). Understanding wormholes in carbonates: Unprecedented experimental scale and 3-D visualization. *Journal of Petroleum Technology, 62*, 78–81.

Meakin, P. (1998). *Fractals. Scaling and Growth Far From Equilibrium*. Cambridge University Press.

Merino, E., & Banerjee, A. (2008). Terra Rossa genesis, implications for Karst, and Eolian dust: A geodynamic thread. *The Journal of Geology, 116*, 62–75.

Merino, E., & Canals, A. (2011). Self-accelerating dolomite-for-calcite replacement: Self-organized dynamics of burial dolomitization and associated mineralization. *American Journal of Science, 311*, 572–607.

Morawiecka, I., & Walsh, P. (1997). A study of solution pipes preseryed in the Miocene limestones (Staszów, Poland). *Acta Carsologica, 20*, 337–350.

Motyka, I., & Wilk, Z. (1984). Hydraulic structure of karst-fissured Triassic rocks in the vicinity of Olkusz (Poland). *Kras i Speleologia, 14*, 11–24.

Muskat, M. (1937). *Flow of homogeneous fluids through porous media*. McGraw-Hill Book Company.

Noiriel, C., & Deng, H. (2018). Evolution of planar fractures in limestone: The role of flow rate, mineral heterogeneity and local transport processes. *Chemical Geology, 497*, 100–114.

Noiriel, C., Luquot, L., Madé, B., Raimbault, L., Gouze, P., & van der Lee, J. (2009). Changes in reactive surface area during limestone dissolution: An experimental and modelling study. *Chemical Geology, 265*, 160–170.

Ortoleva, P., Chadam, J., Merino, E., & Sen, A. (1987). Geochemical self-organization II: The reactive-infiltration instability. *American Journal of Science, 287*, 1008–1040.

Ortoleva, P. J. (1994). *Geochemical self-organization*. New York: Oxford University Press.

Osselin, F., Budek, A., Cybulski, O., Kondratiuk, P., Garstecki, P., & Szymczak, P. (2016). Microfluidic observation of the onset of reactive infiltration instability in an analog fracture. *Geophysical Research Letters, 43*, 6907–6915.

Ott, H., & Oedai, S. (2015). Wormhole formation and compact dissolution in single-and two-phase CO_2-brine injections. *Geophysical Research Letters, 42*, 2270–2276.

Paillet, F. L., Hess, A. E., Cheng, C. H., & Harding, E. (1987). Characterization of fracture permeability with high-resolution vertical flow measurements during borehole pumping. *Ground Water, 25*, 28–40.

Palmer, A. N. (1991). Origin and morphology of limestone caves. *Geological Society of America Bulletin, 103*, 1–21.

Paterson, L. (1981). Radial fingering in a Hele-Shaw cell. *Journal of Fluid Mechanics, 113*, 513–529.

Plummer, L. N., & Wigley, T. L. M. (1976). The kinetics of calcite dissolution in CO_2-water systems at 25C and 1 atmosphere total pressure. *Geochimica et Cosmochimica Acta, 40*, 191–202.

Plummer, L. N., Wigley, T. L. M., & Parkhurst, D. L. (1978). The kinetics of calcite dissolution in CO_2-water systems at 5C to 60C and 0.0 to 1.0 atm of CO_2. *American Journal of Science, 278*, 179–216.

Prestwich, J. (1855). On the origin of the sand-and gravel-pipes in the chalk of the London tertiary district. *Quarterly Journal of the Geological Society, 11*(1–2), 64–84.

Putnis, A. (2009). Mineral replacement reactions. *Reviews in Mineralogy and Geochemistry, 70*(1), 87–124.

Saffman, P. G., & Taylor, G. I. (1958). The penetration of a fluid into a porous medium or Hele-Shaw cell containing a more viscous liquid. *Proceedings of the Royal Society of London. Series A, 245*(1242), 312–329.

Selvadurai, A. P. S., Couture, C.-B., & Rezaei Niya, S. M. (2017). Permeability of wormholes created by CO_2-acidized water flow through stressed carbonate rocks. *Physics of Fluids, 29*, 096604.

Shalev, E., Lyakhovsky, V., & Yechieli, Y. (2006). Salt dissolution and sinkhole formation along the Dead Sea shore. *Journal of Geophysical Research, 111*, B03102.

Sharp, I., Gillespie, P., Morsalnezhad, D., Taberner, C., Karpuz, R., Vergés, J., Horbury, A., Pickard, N., Garland, J., & Hunt, D. (2010). Stratigraphic architecture and fracture-controlled dolomitization of the Cretaceous Khami and Bangestan groups: an outcrop case study, Zagros Mountains, Iran. *Geological Society Special Publication, 329*, 343–396.

Sherwood, J. D. (1987). Stability of a plane reaction front in a porous medium. *Chemical Engineering Science, 42*, 1823–1829.

Smith, M. M., Sholokhova, Y., Hao, Y., & Carroll, S. A. (2013). CO_2-induced dissolution of low permeability carbonates. Part I: Characterization and experiments. *Advances in Water Resources, 62*, 370–387.

Snippe, J., Berg, S., Ganga, K., Brussee, N., & Gdanski, R. (2020). Experimental and numerical investigation of wormholing during CO_2 storage and water alternating gas injection. *International Journal of Greenhouse Gas Control, 94*, Article 102901.

Steefel, C. I., Molins, S., & Trebotich, D. (2013). Pore scale processes associated with subsurface CO_2 injection and sequestration. *Reviews in Mineralogy and Geochemistry, 77*, 259–303.

Szymczak, P., & Ladd, A. J. C. (2006). A network model of channel competition in fracture dissolution. *Geophysical Research Letters, 33*, L05401.

Szymczak, P., & Ladd, A. J. C. (2011). The initial stages of cave formation: Beyond the one-dimensional paradigm. *Earth and Planetary Science Letters, 301*, 424–432.

Szymczak, P., & Ladd, A. J. C. (2011). Instabilities in the dissolution of a porous matrix. *Geophysical Research Letters, 38*, L07403.

Szymczak, P., & Ladd, A. J. C. (2012). Reactive infiltration instabilities in rocks. Fracture dissolution. *Journal of Fluid Mechanics, 702*, 239–264.

Szymczak, P., & Ladd, A. J. C. (2013). Interacting length scales in the reactive-infiltration instability. *Geophysical Research Letters, 40*, 3036–3041.

Szymczak, P., Kwiatkowski, K., Jarosinski, M., Kwiatkowski, T., & Osselin, F. (2019). Wormhole formation during acidizing of calcite-cemented fractures in gas-bearing shales. *SPE Journal, 24*(02), 795–810.

Tang, M., Wu, Z., Wang, A., Zuo, Y., Lou, Y., Liu, H., & Sun, W. (2021). Study on the microscopic fracture process and acoustic emission of shale based on digital image. *Geofluids, 2021*, 8874918.

Trimmer, J. (1845). On the pipes or sand-galls in the chalk and chalk-rubble of Norfolk. *Quarterly Journal of the Geological Society of London, 1*, 300–317.

Tsai, V. C., & Wettlaufer, J. S. (2007). Star patterns on lake ice. *Physical Review E, 75*, Article 066105.

Walsh, P., & Morawiecka-Zacharz, I. (2001). A dissolution pipe palaeokarst of mid-Pleistocene age preserved in Miocene limestones near Staszów, Poland. *Palaeogeography, Palaeoclimatology, Palaeoecology, 174*(4), 327–350.

White, W. B. (1977). Role of solution kinetics in the development of karst aquifers. *Memoirs of the International Association of Hydrogeologists, 12*, 503–517.

White, W. B., & Longyear, J. (1962). Some limitations on speleogenetic speculation imposed by the hydraulics of groundwater flow in limestone. *Nittany Grotto, 10*, 155–167.

Witten, T. A., & Sander, L. M. (1981). Diffusion-limited aggregation, a kinetic critical phenomenon. *Physical Review Letters, 47*, 1400.

Wooding, R. A. (1969). Growth of fingers at an unstable diffusing interface in a porous medium or Hele-Shaw cell. *Journal of Fluid Mechanics, 39*, 477–495.

Zik, O., Olami, Z., & Moses, E. (1998). Fingering instability in combustion. *Physical Review Letters, 81*(18), 3868–3871.